

# Alaska Upper Crustal Velocities Revealed by Air-to-Ground Coupled Waves From the 2022 Hunga Tonga–Hunga Ha’apai Eruption

Kenneth A. Macpherson \*<sup>1</sup>, David Fee <sup>1</sup>, Stefan Awender <sup>1</sup>, Bryant Chow <sup>1</sup>, Juliann Colwell <sup>1</sup>, Sam Delamere <sup>1</sup>, Mathew Haney <sup>2</sup>

<sup>1</sup>Wilson Alaska Technical Center, Geophysical Institute, University of Alaska Fairbanks, 2156 Koyukuk Drive, Fairbanks, Alaska, U.S.A., <sup>2</sup>Alaska Volcano Observatory, U.S. Geological Survey, Anchorage, Alaska, U.S.A

**Author contributions:** *Conceptualization:* Kenneth A. Macpherson, David Fee. *Formal Analysis:* Kenneth A. Macpherson, David Fee, Stefan Awender, Bryant Chow, Juliann Colwell, Sam Delamere, Mathew Haney. *Writing - Original draft:* Kenneth Macpherson. *Writing - Review & Editing:* Kenneth A. Macpherson, David Fee, Stefan Awender, Bryant Chow, Juliann Colwell, Sam Delamere, Mathew Haney. *Project administration:* David Fee.

**Abstract** Pressure changes in the atmosphere couple to the solid Earth, producing ground motions that contain information about local crustal elastic parameters. This type of air-to-ground coupled wave was observed globally following the largest explosion of the instrumental age, the climactic eruption of the Hunga Tonga–Hunga Ha’apai volcano on 15<sup>th</sup> January, 2022. We utilize this unprecedented source, along with the presence of colocated seismometers, infrasound sensors, and barometers in Alaska, to examine coupling and reveal elastic parameters beneath the stations. We derive coupling spectra by forming seismic-to-pressure amplitude ratios as a function of frequency, and identify passbands of high coherence between the pressure and seismic records. By relating coupling spectra in high-coherence bands to elastic parameters, we estimate mean shear wave velocities under stations to a depth encompassing much of the upper crust. Our velocity estimates from low-frequency coupling exhibit good agreement with a previously existing tomographic velocity model from Berg et al. (2020), while estimates from high-frequency coupling show considerable scatter when compared to proxy  $V_{s30}$ , even though the overall values are reasonable. In addition to providing velocity estimates, our results also indicate that, for the broadband pressure signals from the Hunga Tonga–Hunga Ha’apai eruption, microseismic noise exerts a strong effect on the frequency bands where coupling is observed, and that the air-to-ground coupled waves exhibit significant complexity not necessarily described by theory. Our results show that coupling observations provide a simple forward observation of mean seismic velocities beneath seismoacoustic stations, without the need to resort to complex inversion schemes. It is remarkable that pressure waves generated thousands of kilometers away are able to reveal the seismic velocity structure of Alaska to several kilometers depth.

Production Editor:  
Yen Joe Tan  
Handling Editor:  
György Hetényi  
Copy & Layout Editor:  
Hannah F. Mark

Signed reviewer(s):  
Toshiro Tanimoto  
Ronan LeBras

Received:  
January 17, 2025  
Accepted:  
May 15, 2025  
Published:  
July 8, 2025

## 1 Introduction

When a pressure wave in the atmosphere interacts with the solid earth, a fraction of the energy from that wave is transferred to the ground as seismic waves—a process known as air-to-ground coupling (Sabatier et al., 1986). This phenomenon, which we refer to simply as “coupling” below, has been considered as both a source of noise to be mitigated or as signal to be exploited, depending on the perspective of the observer (Dugick et al., 2023). Coupling has long been of interest to seismologists from the perspective of data quality. Atmospheric pressure variations are detectable on broadband seismometers, and these so-called pressure effects typically present at long periods (>100 sec), particularly on horizontal channels, and are generally considered by seismologists to be noise (Sorrells, 1971; Beauduin et al., 1996; Alejandro et al., 2020). There has been considerable effort undertaken to understand and mitigate these effects. The theory developed by Sor-

rells (1971) describing the response of an elastic half space to a plane pressure wave illustrated that coupled waves decay rapidly with depth, indicating that placing seismometers in boreholes can effectively mitigate this source of noise. Tanimoto and Valovcin (2016) used pressure perturbations from two tropical cyclones recorded on colocated pressure and seismic sensors to define a threshold pressure below which the vertical component of a broadband seismometer is unaffected. Additional mitigation efforts include removing the long-period pressure-induced noise in processing via the application of a pressure-to-seismic transfer function and insulating seismic installations from pressure changes (Beauduin et al., 1996; Ringler et al., 2019).

While coupled waves can be a source of seismic noise, they may also be considered signal, and the coupling phenomenon has been leveraged to use seismic networks as ad hoc low-frequency acoustic networks (Anglin and Haddon, 1987). For example, Langston (2004) used three-component seismic stations in the southeastern United States (US) to study coupled waves in-

\*Corresponding author: kamacpherson@alaska.edu

duced by atmospheric shockwaves associated with the 3<sup>rd</sup> November, 2003 bolide. The deployment of the EarthScope USArray Transportable Array (TA) to the contiguous United States and Alaska, beginning in 2004, resulted in a relatively dense grid of stations across the region, which have been used to study low-frequency acoustic waves (Meltzer et al., 1999; Tyttell et al., 2016). For example, Walker et al. (2011) used coupled waves recorded on TA stations in the western US to compile a catalog of infrasound (acoustic waves with frequencies below 20 Hz) sources using reverse time migration. In addition to regional studies, coupled waves recorded on seismic networks local to volcanoes have been used to enhance detection and characterization of volcanic eruptions (Fee et al., 2016). The AlpArray seismic network in Germany recorded coupled waves from a 2018 refinery explosion, and these observations were used along with ray-tracing to identify different infrasound phases (Fuchs et al., 2019). Seismoacoustic stations, that is, stations equipped with colocated seismic and pressure sensors, are of particular utility for studying coupled waves. Three-component seismic sensors colocated with pressure sensors that record coupled waves have been used to estimate the back azimuth to the pressure source. This has been accomplished by examining the phase shift imposed by the small spatial offsets between the sensors (McKee et al., 2018), or by minimizing the coherence with the pressure time series by rotating a horizontal seismic component until it is at a direction transverse to the source (Bishop et al., 2023).

Coupled waves are intrinsically related to the material parameters of the ground. The theory for the displacement of an elastic half space in response to a pressure source moving at typical wind velocities ( $\leq 20$  m/s) derived by Sorrells (1971) was generalized by Ben-Menahem and Singh (1981) to include sources moving near the speed of sound, provided the source velocity is below the local shear-wave velocity. The theory shows that the displacements are dependent on the elastic parameters of the half space, making it a useful construct for estimating material parameters (Langston, 2004). Using wind as the pressure source, Tanimoto and Wang (2019) extended the theory to a layered half space and presented a scheme to invert seismic-to-pressure amplitude ratios, referred to as coupling ratios, for the elastic parameters of the layers beneath stations with colocated pressure sensors and seismometers. Coupling observations were used along with a simplified version of the Ben-Menahem and Singh (1981) theory to estimate mean material rigidity to a depth of 30 m beneath colocated stations in the eastern US and Alaska (Wang and Tanimoto, 2020). The dependence of coupling ratios on geological conditions has also been indicated by a relationship between the degree of coupling and topographic elevation, which is likely acting as a proxy for the near-surface shear-wave velocity (Wills et al., 2022). The global pressure waves induced by the 2022 climactic eruption of the Hunga Tonga–Hunga Ha’apai volcano were used by Anthony et al. (2022a) to model coupling at long periods (90 sec) on the Global Seismographic Network (GSN). Their study demonstrated that seismic waves were efficiently excited at this period, vibrating

the upper crust to a depth of at least five kilometers.

The fact that the shallow elastic parameter estimation achieved by Tanimoto and Wang (2019) and Wang and Tanimoto (2020) utilized wind as a source restricted the depth sensitivity of the calculation to a few tens of meters. However, the work of Anthony et al. (2022a) demonstrated the depth sensitivity of the pressure perturbations induced by the 2022 Hunga Tonga–Hunga Ha’apai eruption to be two orders of magnitude deeper. In this study, we leverage the unprecedented pressure source from the Hunga Tonga–Hunga Ha’apai eruption, recorded by a regional seismoacoustic network thousands of kilometers away in Alaska, to estimate the mean seismic shear wave velocities ( $V_s$ ) of the upper crust to a depth of five kilometers. We believe that coupling observations have not been used to estimate velocities to such a depth by previous studies. We show that the frequencies at which coupling is most readily observed for this event are controlled by the ambient seismic background noise level. By isolating three different frequency bands where we will show that strong coupling was observed, spanning 0.007 to 1.6 Hz (142 to 0.625 sec), we can obtain mean  $V_s$  estimates for three different depths, including much of the upper crust. We assess the accuracy of our estimates by comparing them to a previously computed model of  $V_{s30}$  and to an upper crustal model of  $V_s$  from tomography. Finally, we discuss some unique features of the Hunga Tonga–Hunga Ha’apai coupled waves in Alaska, and demonstrate that the theory of Sorrells (1971), Ben-Menahem and Singh (1981), and Tanimoto (2024) may not be adequate to describe the observed complexity.

## 1.1 The climactic Hunga Tonga–Hunga Ha’apai eruption

The largest atmospheric explosion of the instrumental age began at approximately 04:00 Coordinated Universal Time (UTC) on 15<sup>th</sup> January, 2022, with an initially submarine eruption of the Hunga Tonga–Hunga Ha’apai volcano in the Kingdom of Tonga (below, we refer to this event as “HTHH”) (Matoza et al., 2022). This was the climactic event of an eruptive episode that began on December 19<sup>th</sup>, 2021, and was extremely energetic, generating a suite of pressure waves across an exceptionally broad spectrum. These included acoustic waves into the audible range ( $> 20.0$  Hz) at source–receiver offsets in excess of 10,000 km and broadband infrasound (0.01 to 20 Hz) that were globally detected. Perhaps the most salient phase generated by the eruption was the Lamb wave—an acoustic gravity wave that propagates in the solid earth–atmospheric waveguide at mean lower-atmospheric wave speeds (Lamb, 1881). Lamb waves are associated with exceptionally large atmospheric explosions and have periods longer than 100 sec. The Lamb wave from the HTHH eruption was observed to make four full passages of the earth, the same number recorded for the Lamb wave produced by the enormous Krakatau eruption in the 19<sup>th</sup> century (Matoza et al., 2022). Pressure waves from the HTHH eruption in both the infrasonic and Lamb frequency bands induced coupling and were recorded on seismometers

(Matoza et al., 2022; Anthony et al., 2022a).

## 1.2 The seismoacoustic network in the Alaska region

The Alaska Earthquake Center and the Alaska Volcano Observatory operate regional networks (network codes AK, and AV, respectively) of colocated broadband seismometers, infrasound sensors, and long-period barometric transducers (barometers) (Alaska Earthquake Center, Univ. of Alaska Fairbanks, 1987; Alaska Volcano Observatory/USGS, 1988). Many of these are former temporary TA stations that were adopted into the permanent regional networks (IRIS Transportable Array, 2003; Meltzer et al., 1999; Busby and Aderhold, 2020). On 15<sup>th</sup> January, 2022, when pressure waves from the HTHH eruption arrived in the region, 150 stations were operating colocated pressure sensors and broadband seismometers. These included 106 network AK stations operating all three sensor platforms of a seismometer, infrasound sensor, and barometer. Network AV provided 44 stations with seismometers and infrasound sensors, ten of which also included barometers. The seismometers are either three-component Kinematics Streckeisen STS-5A or Nanometrics Trillium 120 sampling at 40.0 or 50.0 samples per second (sps). All AK network infrasound sensors and 10 network AV sensors were Hyperion Technology Group IFS-4132 models sampling at 40.0 sps with a flat response from 0.02 Hz up to the Nyquist frequency (Merchant, 2015). The Hyperion infrasound sensors are ported to the atmosphere through a diffuser, which is a polyvinyl chloride cap with small holes around its circumference. The remainder of the network AV infrasound sensor were a variant of the Chaparral 64, either the UHP, UHP2, or Vx2. These have a flat response from 0.02 Hz to the Nyquist frequency, and were sampling at 50 sps. Because TA stations were deployed in Alaska to conform to a geographic grid with roughly 80 km spacing, many are situated in exposed areas and are subject to significant wind-induced noise affecting the infrasound sensors, which are not equipped with wind noise reduction systems (Macpherson et al., 2022). However, the large amplitudes of the HTHH pressure waves allowed them to be well-recorded at the majority of these stations, although several did not record in real-time as they were in their winter power-saving mode. Many of these have since been manually backfilled. The outside ambient pressure at 116 of these stations is recorded by Setra 278 barometers. These are sampled at 40.0 sps and have a flat response below 5.0 Hz. The Hyperion and Setra pressure sensors in former TA stations were chosen to provide a very broadband sampling of the pressure field, as the flat portion of their responses overlap (Tytell et al., 2016).

The combination of the pressure sensor-equipped stations from AK and AV provide a relatively dense, regional seismoacoustic network with extensive geographic coverage of the Alaska region, as can be seen in Figure 1. The figure shows the station distribution, with isolines noting the approximate distance to the HTHH volcanic complex. Stations are colored by the maxi-

imum peak-to-peak amplitude of the HTHH pressure wave recorded on the infrasound sensors, filtered between 0.015 to 0.035 Hz. The inset globe shows the approximate location of the volcano and its relation to the Alaska region. Note the high pressure amplitudes, some in excess of 60 Pa, despite the very large distance to the source. The network recorded high-quality time series of HTHH pressure waves and the resulting coupled seismic waves. This is demonstrated by the high degree of correlation, visible by inspection, between the pressure and vertical seismic time series; we show record sections of waveforms from HTHH recorded on the network in Figure 2a, with vertical seismic channels in red, and infrasound in blue in Figure 2b, filtered between 0.015 and 0.035 Hz. Note the remarkable similarity of the infrasound and seismic waveforms, indicating the latter is indeed the coupled wave. These high-quality recordings of the HTHH eruption provide a unique opportunity to estimate seismic velocities of the upper crust in the Alaska region using coupling observations.

## 2 Methods

While the large amplitudes of the HTHH pressure waves in the Alaska region generally resulted in recordings with good signal-to-noise ratios (see Fig. 1), we need to identify frequency bands where efficient coupling occurred. To do this, we compute the magnitude squared coherence, referred to as “coherence” below, between recorded pressure amplitudes and the corresponding seismic velocity from the vertical components of colocated seismometers. The coherence is given by

$$\gamma^2 = \frac{\overline{G_{PS}}^2}{\overline{G_{PP}} \overline{G_{SS}}}, \quad (1)$$

where  $\overline{G_{PS}}$  is the the cross spectral density of the pressure and seismic data,  $\overline{G_{PP}}$  is the auto spectral density of the pressure data, and  $\overline{G_{SS}}$  is the auto spectral density of the seismic data (Gabrielson, 2011). We assume frequencies with high ( $\geq 0.8$ ) coherence between pressure and seismic indicate robust coupling (Tanimoto and Wang, 2019; Wang and Tanimoto, 2020; Anthony et al., 2022a). We compute power spectral densities (PSD) from the HTHH pressure and seismic waveforms to further investigate the relationships between frequency, amplitudes, and coherence, and to help identify bands with strong coupling. To window the HTHH waveforms for computing coherence and PSDs, we estimate the arrival time by 1) using the origin time of 15<sup>th</sup> January, 2022 04:14:45 UTC from Matoza et al. (2022); 2) computing the source–receiver offset using the World Geodetic System 1984 ellipsoid (Slater and Malys, 1998); and 3) finding the approximate arrival time at each station assuming a mean celerity of 320 m/s (Matoza et al., 2022). We then take a 2-hour window from this arrival time for analysis. For both the PSD and coherence calculations, we divide the data into 5 segments for frequencies higher than 0.015 Hz or 3 segments for frequencies below 0.015 Hz, and use an overlap of 75% (Welch, 1967). Before computing PSDs, we remove the instrument response of each waveform so

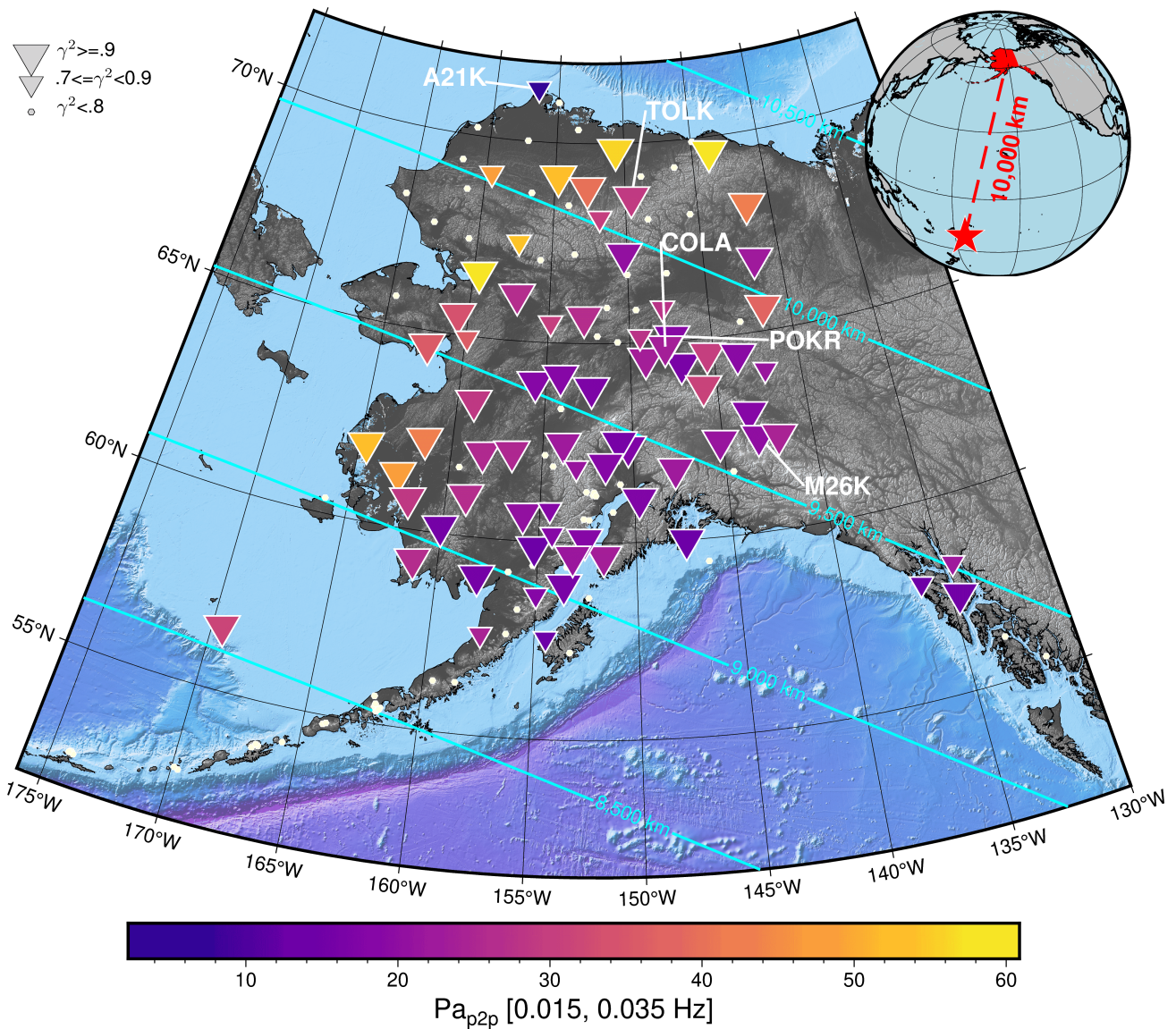


**Figure 1** Map of Alaska showing stations with colocated broadband seismometers and pressure sensors that recorded signal from the HTHH eruption with high ( $\geq 0.8$ ) coherence between the vertical seismic and infrasound in a 0.015 to 0.035 Hz passband. The approximate location of the HTHH volcano is shown by the red star in the inset. Contours show approximate distance from the volcano. Stations with high coherence are colored by maximum pressure peak-to-peak amplitude. Station symbol sizes correspond to average coherence for the band. Stations mentioned explicitly in the text are annotated.

that seismic data are in velocity with units of m/s, and pressure data have units of Pa.

We show the output from the coherence and PSD calculation for all stations in Figure 3. The seismic PSDs are shown in red, the pressure in blue, and the coherence in gray. Bright red, blue, and gray lines are the stacked seismic PSDs, pressure PSDs, and coherence, respectively. Pressure data from the infrasound sensors for frequencies between 0.01 and 2.0 Hz are shown in Figure 3a, while pressure data from the barometers for frequencies between 0.007 and 0.013 Hz are shown in Figure 3b. The seismic data in both Figures 3a and 3b are from the vertical component of the broadband seismometers. This figure provides a broadband, network view of coherence and amplitudes from the HTHH pressure waves, and several features stand out. There is an obvious coherence peak at 0.025 Hz, indicating strong coupling at this frequency. Addition-

ally, there is a modest coherence plateau above 1.0 Hz, where some stations exhibit high coherence while others do not. This large scatter in high-frequency coherence across the network results in modest ( $\approx 0.5$ ) values for the stack of network coherence. Coherence drops to nearly zero in a band centered around 0.2 Hz (5.0 sec), corresponding to the secondary microseism; likely a result of the microseismic amplitudes exceeding those of the coupled wave. There is also a local minimum of coherence around 0.08 Hz (12.5 sec), likely imposed by the relatively high seismic amplitudes from the primary microseism (McNamara and Buland, 2004). These dips in coherence indicate that bands where coupling is observed for this event, even though pressure amplitudes are large, are predominantly controlled by the ambient seismic noise level. This supports the observation of Anthony et al. (2022a) that maximum observed coupling occurred on the GSN on the quietest

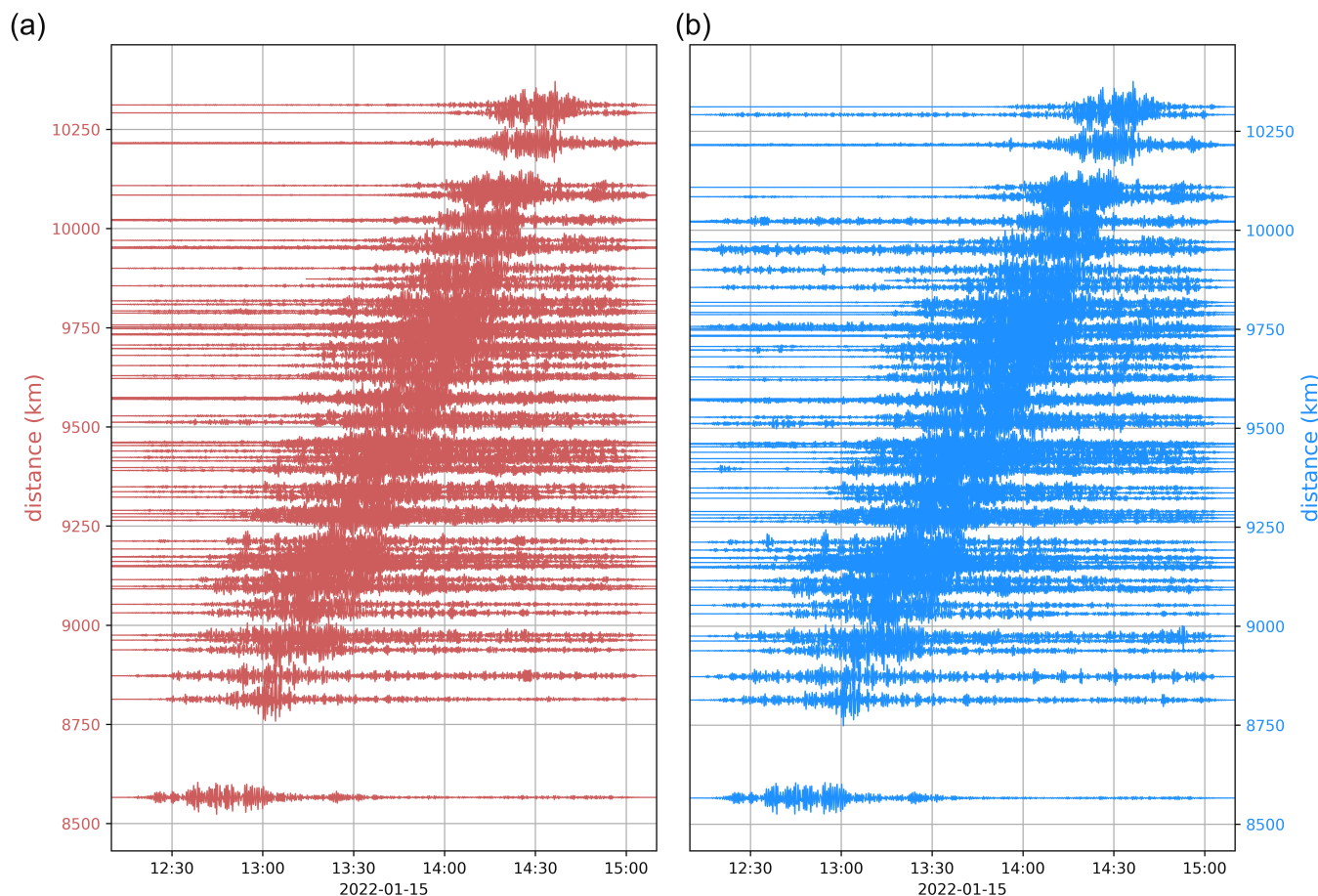


**Figure 2** Record section of waveforms from the HTHH explosion recorded on the Alaska regional seismoacoustic network (see Fig. 1). All waveforms have been filtered between 0.015 and 0.035 Hz and the amplitudes of each trace have been normalized. (a) Recordings from vertical seismic channels in red. (b) Recordings from infrasound channels in blue.

portion of the seismic noise spectrum. It also may be the case that the band near 0.025 Hz is dominated by the crustal Airy phase, where Rayleigh wave amplitudes are enhanced by constructive interference imposed by a crustal waveguide (Aki and Richards, 2002). Below the 0.025 Hz peak, coherence gradually decreases with decreasing frequency, but there is still good coherence below the infrasound band ( $< 0.01$  Hz). There is a modest local maximum in coherence at 0.00975 Hz (102.0 sec), indicating strong low-frequency coupling in the Alaska region. Based on this coherence analysis, we investigate three different bands in which strong coupling is indicated; 1.2 to 1.6 Hz (0.83 to 0.625 sec), 0.015 to 0.035 Hz (66.6 to 28.6 sec), and 0.007 to 0.0125 Hz (142.85 to 80.00 sec) (Fig. 3).

Tanimoto and Wang (2019) provide a general “rule of thumb” expression for the average depth sensitivity of elastic parameters to pressure–seismic coupling as a function of frequency, allowing us to interpret these frequency bands as proxies for depth. The depth sensitivity is given by

$$h = 0.15 \cdot c \cdot T, \quad (2)$$

where  $h$  is depth in meters,  $c$  is the mean pressure source speed in m/s, and  $T$  is the period in seconds. Here we assume that the pressure source speed is equal to the local sound speed, which may be estimated as a

function of temperature. We use a linear approximation of the speed of sound in an ideal gas, valid for temperatures between  $-33$  and  $77$  degrees Celsius ( $^{\circ}\text{C}$ ), given by  $c = 331.3 \text{ m/s} + 0.6 \text{ m/s/}^{\circ}\text{C} \times \text{Temp}$  where  $\text{Temp}$  is the local air temperature in  $^{\circ}\text{C}$  (Kinsler, 2000).

We downloaded mean hourly surface temperature data for the Alaska region from the ERA5 reanalysis product from the European Centre for Medium-Range Weather Forecasts (Zippenfenig, 2023; Hersbach et al., 2023). These data indicate that the mean temperature across the state of Alaska around the time of the HTHH arrivals was  $\approx -13.6^{\circ}\text{C}$ , which corresponds to a mean sound speed of 323.0 m/s. To estimate the depths to which we are computing average velocities, we use equation 2 with a mean sound speed of 323.0 m/s and the mean frequency of each pass band. This results in approximate depths of 35 m (1.2–1.6 Hz), 1,900 m (0.015–0.035 Hz) or 2 km, and 4,900 m (0.007–0.0125 Hz) or 5 km. It is remarkable that the crust is sensitive to an atmospheric pressure wave to a depth of nearly 5 km, particular since the theory of Sorrells (1971) shows that the coupled wave attenuates exponentially with depth.

In the analysis below, we express seismic-to–pressure coupling ratios as functions of frequency by taking ratios of PSDs. We refer to these ratios as coupling spectra. Specifically, we define the coupling spectra as the square root of the ratio of the seismic

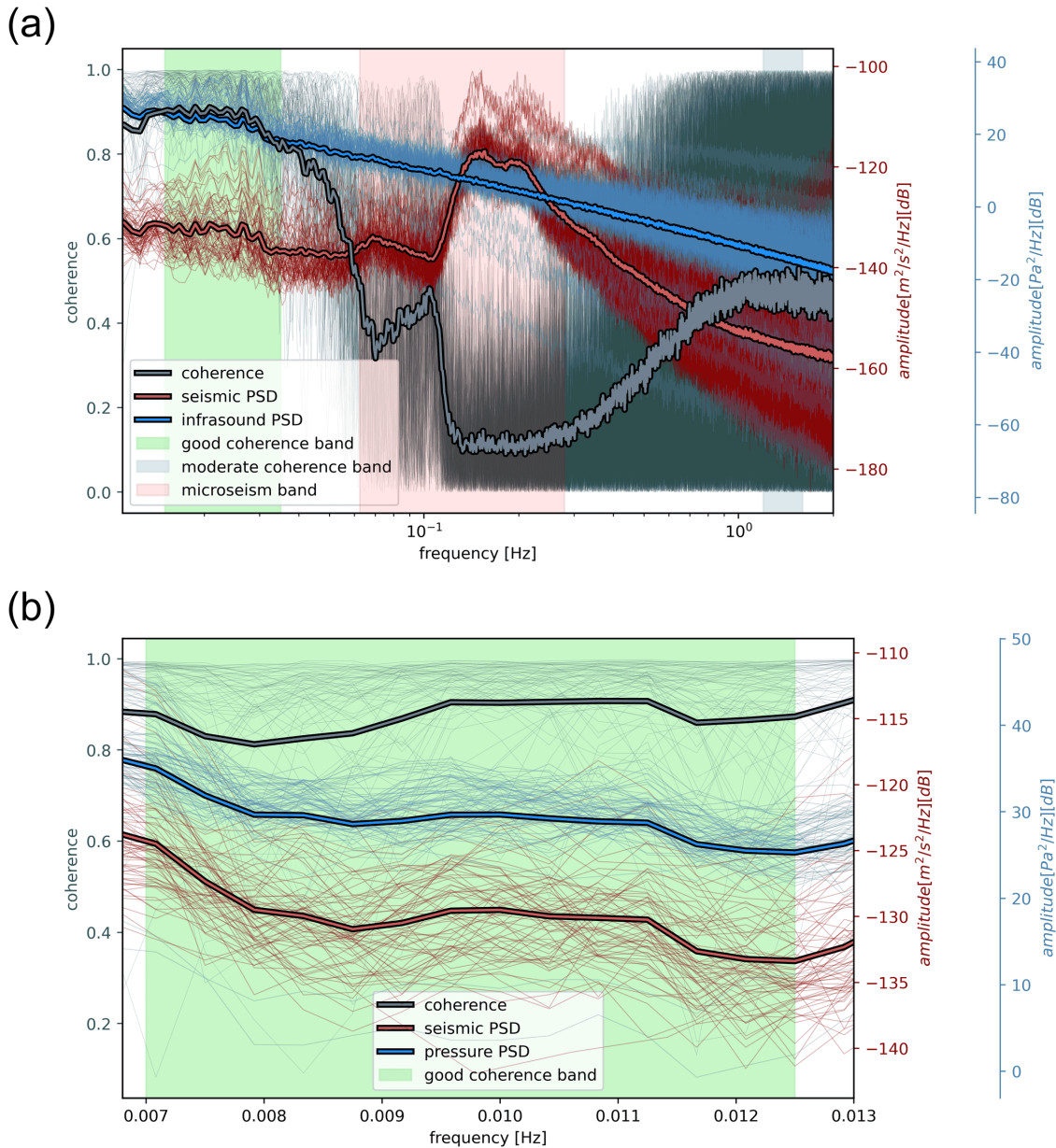


**Figure 3** Network view of pressure and vertical seismic amplitudes and pressure-seismic coherence as functions of frequency for two hours of data starting a few minutes before the HTHH arrivals. Seismic power spectral densities (PSDs) are shown in red, pressure PSDs are shown in blue, and coherence is shown in gray for individual stations. The thick traces are stacks of all station PSDs and coherence curves. The microseism band and target bands of good or moderate coherence are shown by red, green, and blue boxes, respectively. (a) The top panel shows from 0.01 to 2.0 Hz and uses the pressure recorded on infrasound channels. (b) The lower panel shows from 0.007 to 0.013 Hz and uses the pressure recorded on the barometer channels. Note that the horizontal axis of panel a) is a log scale while panel b) uses a linear scale.

PSD to the pressure PSD, i.e.

$$\Gamma(f) = \sqrt{\frac{PSD_s(f)}{PSD_p(f)}}, \tag{3}$$

where  $f$  is frequency,  $PSD_s$  is the seismic PSD (velocity), and  $PSD_p$  is the pressure PSD (Wills et al., 2022) and has units of  $m/(Pa \cdot s)$ . The coupling ratio for the band pass of interest is simply the mean of the coupling spectra in that band,

$$\bar{\Gamma} = \text{mean}(\Gamma[f_1, f_2]), \tag{4}$$

where  $f_1$  and  $f_2$  are the frequency bounds.

In order to estimate the mean seismic velocity to the depths associated with the three bands outlined above, we use the theory of Sorrells (1971) for the response of an elastic half space that relates the coupling ratio of vertical seismic velocity to pressure with the Lamé parameters,

$$\bar{\Gamma} = \frac{c(\lambda + 2\mu)}{2\mu(\lambda + \mu)}, \tag{5}$$

where  $c$  is the source velocity, or the sound speed in our case,  $\lambda$  is the first Lamé parameter, and  $\mu$  is the rigidity. Note that  $\mu$  and  $\lambda$  both have units of Pa, so that equation 5 has units of  $m/(Pa \cdot s)$ , identical to equation 3.

Although there is a companion expression relating the coupling ratio of radial seismic velocity and pressure to the elastic parameters, we do not use this expression due to weaker and more variable coherence between radial seismic and pressure, which we discuss in more detail below. Consequently, with only equation 5, we have a single equation with two unknowns. To simplify this, we follow the method of Wang and Tanimoto (2020), in which they define a “modified” rigidity,  $\bar{\mu}$ , under the assumption that  $\lambda \gg \mu$  in the upper crust. The modified rigidity is given by

$$\bar{\mu} = \frac{\lambda + \mu}{\lambda + 2\mu} \mu. \quad (6)$$

By substituting equation 6 into equation 5, solving for  $\bar{\mu}$ , and assuming that the modified rigidity approximates the true rigidity, we obtain a simplified expression for rigidity as a function of pressure–seismic coupling,

$$\bar{\mu} = \frac{c}{2\Gamma}. \quad (7)$$

This provides a simple, intuitive expression in which rigidity is inversely proportional to the coupling ratio via the sound speed. The equation illustrates that larger coupling values occur in material that is less rigid and thus less resistant to pressure-induced ground motion. Finally, using an independent estimate for mean material density, we can convert our rigidity estimate to shear wave velocity using the well-known expression

$$V_s = \sqrt{\frac{\bar{\mu}}{\rho_{est}}}, \quad (8)$$

where  $\rho_{est}$  is a density estimate of the material (Shearer, 2019).

## 2.1 Existing velocity models for comparison

In order to evaluate the effectiveness of our  $V_s$  estimates derived from coupling observations, we compare our results to existing velocity models for the Alaska region. For our high-frequency band corresponding to an approximate depth of 35 m, the most appropriate existing models are of  $V_{s30}$ , which is the depth-averaged  $V_s$  for the upper 30 m of material. Specifically, we use the Alaska portion of the U.S. Geological Survey’s global  $V_{s30}$  map, referred to below as “ $V_{s30}Model$ ” (Wald and Allen, 2007; Yong et al., 2016; Heath et al., 2020). This map primarily uses topographic slope as a proxy for  $V_{s30}$ , but also smoothly integrates survey data for areas where they are available. Survey data for Alaska are limited to 15 sites, so the bulk of the map for our study area is from the proxy slope value. The original grid has a spatial resolution of 30 arc-seconds, so to compare the model  $V_{s30}$  values to our coupling estimates, we use a bicubic interpolation to sample the model grid at station coordinates.

For our lower frequency bands corresponding to depths of approximately 2 km and 5 km, we compare our estimates to the tomographic model from Berg et al. (2020). Their study utilized TA data to construct a  $V_s$  model for the Alaska region by jointly inverting receiver

functions with Rayleigh wave ellipticity and phase velocity data compiled from earthquakes and ambient noise. The model is particularly well-suited for comparison to our estimates due to its ability to resolve shallow crustal structure, such as basins, along with its good depth resolution. The model consists of 156 layers ranging from the surface to a depth of 144 km. Below 5 km, the layers are 1 km thick, but have 250 m thickness for shallower layers. To find the mean  $V_s$  from this model corresponding to our velocity estimates from coupling, we find the average of the layers, weighted by layer thickness, to the layer depth closest to our target depth. Thus, for our 2 km estimate, we depth-average the model down to the 2 km layer, and for our 5 km estimate, we depth-average down to 5 km. We create new depth-averaged grids of mean  $V_s$  for these depths, and then use bicubic interpolation to sample the grids at station coordinates. We note that original 0.2° by 0.1° grids were interpolated from observations and station locations in order to approximate a 3D model.

The conversion from our modified rigidity calculation to  $V_s$  requires an estimate of material density (see eq. 8). For the estimates to 2 km and 5 km depth, we use a density estimate from a third existing model in order not to bias our  $V_s$  estimate towards the model used for comparison, and because the Berg model does not provide independent estimates of density. For this purpose, we use the CRUST1.0 model, which is a global crustal model with 1° spatial resolution (Laske et al., 2013). The model consists of 8 layers from the surface, including ice and water, down to the lower crust and including the upper mantle. Unlike the Berg et al. (2020) tomographic model, CRUST1.0 provides independent estimates of velocity and density. To find the density we need for use in equation 8, we discretize the model into 100 m slices, following Anthony et al. (2022a), and depth-integrate the density to the appropriate depth. For the 35 m estimate, we use densities from the top layer of the Berg tomographic model, as we expect it to have superior near-surface resolution.

The models introduced above are useful for comparison and provide an indication of the efficacy of using coupling observations from the HTHH pressure waves to estimate mean  $V_s$ . It is important to note that they are models, and should not be considered ground truth. However, we believe it is reasonable to expect at least first-order agreement, and they are therefore useful in assessing our technique’s utility.

## 3 Results

Coupling spectra (eq. 3) for stations in the Alaska region that recorded air-to-ground coupled waves from the HTHH explosion are shown in Figure 4. Specifically, the figure shows frequency as a function of coupling ratio (units of  $m/Pa \cdot s$ ) with the dots colored by coherence. We consider coupling values with a coherence less than 0.8 to have low coherence. These values are indicated as small gray dots and are not used in our calculation of  $V_s$ . The two panels in Figure 4 cover a broad spectrum from 0.0065 to 2.0 Hz, covering much of the infrasound spectrum and below (<0.01 Hz). Coupling cal-

culations displayed on the higher-frequency panel (Fig. 4a) use infrasound channels, while the lower-frequency panel (Fig. 4b) uses barometer channels. The vertical axis labels on the right-hand side of each panel indicate the depth sensitivities corresponding to the frequencies and were computed via equation 2. The blue squares are theoretical coupling values computed via equation 5 using elastic parameters for a central Alaska site (150°W, 65°N) from CRUST1.0.

There are several salient features evident from inspecting the coupling spectra. There is a clear lack of high coherence along with elevated seismic amplitudes in a band corresponding to the secondary microseism, similar to what is observed in Figure 3. This further illustrates the dependence of observable coupling from this event on the ambient seismic noise levels. There is a band of high coherence for almost the entire network between approximately 0.015 and 0.04 Hz, also in agreement with Figure 3. At frequencies above 0.9 Hz there is considerable spread, with some stations exhibiting high coherence and others not, along with a large range of coupling ratios. This likely reflects the large diversity of site conditions for the Alaska regional seismoacoustic network (see Fig. 1), including stations on hard rock, coastal areas, basins, and alluvial valleys, along with variable pressure amplitudes across the state. More generally, for high-coherence values between 0.01 and 2.0 Hz, we observe an approximately log-linear relationship between frequency and coupling ratio. This likely reflects the depth-attenuation implied by Sorrells (1971), as well as indicating that deeper, likely more rigid material is more resistant to coupling, while shallower, seismically slower material is more readily excited by the pressure waves. This supports the simple relationship assumed in equation 6. Observed coupling values are similar in shape to theoretical values, although they tend to be lower. We hypothesize that this is likely due to the poor shallow layer resolution of the CRUST1.0 model. For frequencies below 0.01 Hz shown in Figure 3b, the coupling spectra are generally simpler and match theoretical values more closely. There is generally good coherence below 0.013 Hz, continuing to at least 0.007 Hz.

We use equations 6 and 8, along with coupling values from equation 4, to compute mean  $V_s$  below the Alaska seismoacoustic network to depths of 35 m, 2 km, and 5 km, corresponding to band passes of 1.2 to 1.6 Hz (0.83 to 0.63 sec), 0.015 to 0.035 Hz (66.6 to 28.6 sec), and 0.007 to 0.0125 Hz (142.85 to 80.00 sec), respectively. We find 46 stations with good coherence ( $\geq 0.8$ ) for the 35 m depth, 82 stations with good coherence for the 2 km depth, and 67 stations with good coherence for the 5 km depth.

The results for the  $V_s$  calculation to 35 m are shown in Figure 5. We find a range of reasonable velocities for the upper 35 meters of materials across both soft soil and hard rock sites of between 120 m/s and 2,332 m/s. We show a scatter plot of our  $V_s$  values from coupling as a function of the  $V_{s30}Model$  values in Figure 5a. The best fit line is plotted in purple, and the gray dotted line indicates equality between the independent and dependent variables. Note there is considerable scatter

and a lack of a linear relationship, with an  $R^2$  value of 0.02. Also, our estimates are systematically faster than the  $V_{s30}Model$  values, and many of our  $V_s$  estimates are above the maximum  $V_{s30}Model$  value of 900 m/s. The right panel shows a map view of this data set, with stations indicated with inverted triangles colored by the coupling  $V_s$  estimate and the symbol size scaled by coherence. The background color map is the  $V_{s30}Model$ , using the same colorbar as the coupling  $V_s$  estimate. Again, it is clear from this map that the  $V_s$  from coupling is generally faster, and at some stations significantly so.

The results of estimating mean  $V_s$  to a depth of 2 km using acoustic-seismic coupling are shown in Figure 6. We find generally realistic values for the shallow crust of between 630 m/s and 3600 m/s. This figure setup is similar to Figure 5 with the scatter plot on the left and a spatial view on the right. We observe generally good agreement between our estimates and the Berg et al. (2020) model, depth-averaged to 2 km. We observe a modest correlation between our estimates and the model values, with an  $R^2$  of 0.30. The best-fit lines and the line indicating equality have similar slopes, but indicate that the coupling-derived values are modestly slower. This may be due to the fact that coupling observations are more sensitive to slow, near-surface layers (Tanimoto and Wang, 2019). Our estimates agree with the Berg model on some broad features, such as the slower material of the North Slope basin (north of  $\approx 68^\circ$ ) and another low-velocity zone in the vicinity of Cook Inlet basin (near 151°W, 60°N). Note that the very low velocity (630 m/s) station, station A21K (see Fig. 1), is in the North Slope basin area and is a known soft-soil site. The regional network typically excludes timing from this station in their earthquake locations due to highly delayed arrival times. Further note that this station is excluded from the scatter plot, as there is no corresponding value from the Berg model.

We show similar plots for the 5 km depth  $V_s$  results in Figure 7. Our estimates provide generally realistic values for the upper crust of between approximately 2,300 m/s and 3,500 m/s. For this depth we again observe lower  $V_s$  values from coupling than those of the Berg model, but we see a modest relationship between the observations and model, with an  $R^2$  of 0.37. Our estimates again capture some large-scale features that are present in the Berg model, such as low velocity zones associated with the North Slope basin, the Cook Inlet basin, and the Cape Yakataga region (145°W, 60°N). Stations in the North Slope Basin area exhibit velocities around 2,400 m/s while Cook inlet and Cape Yakataga sites are moderately faster at around 2,600 m/s. These are in contrast to many interior sites, which exhibit velocities in excess of 3,000 m/s.

## 4 Discussion

### 4.1 Observational departures from theory

The theory expounded in Sorrells (1971) and Ben-Menahem and Singh (1981) makes several predictions that have been studied by other researchers and can be further investigated via the seismoacoustic waves

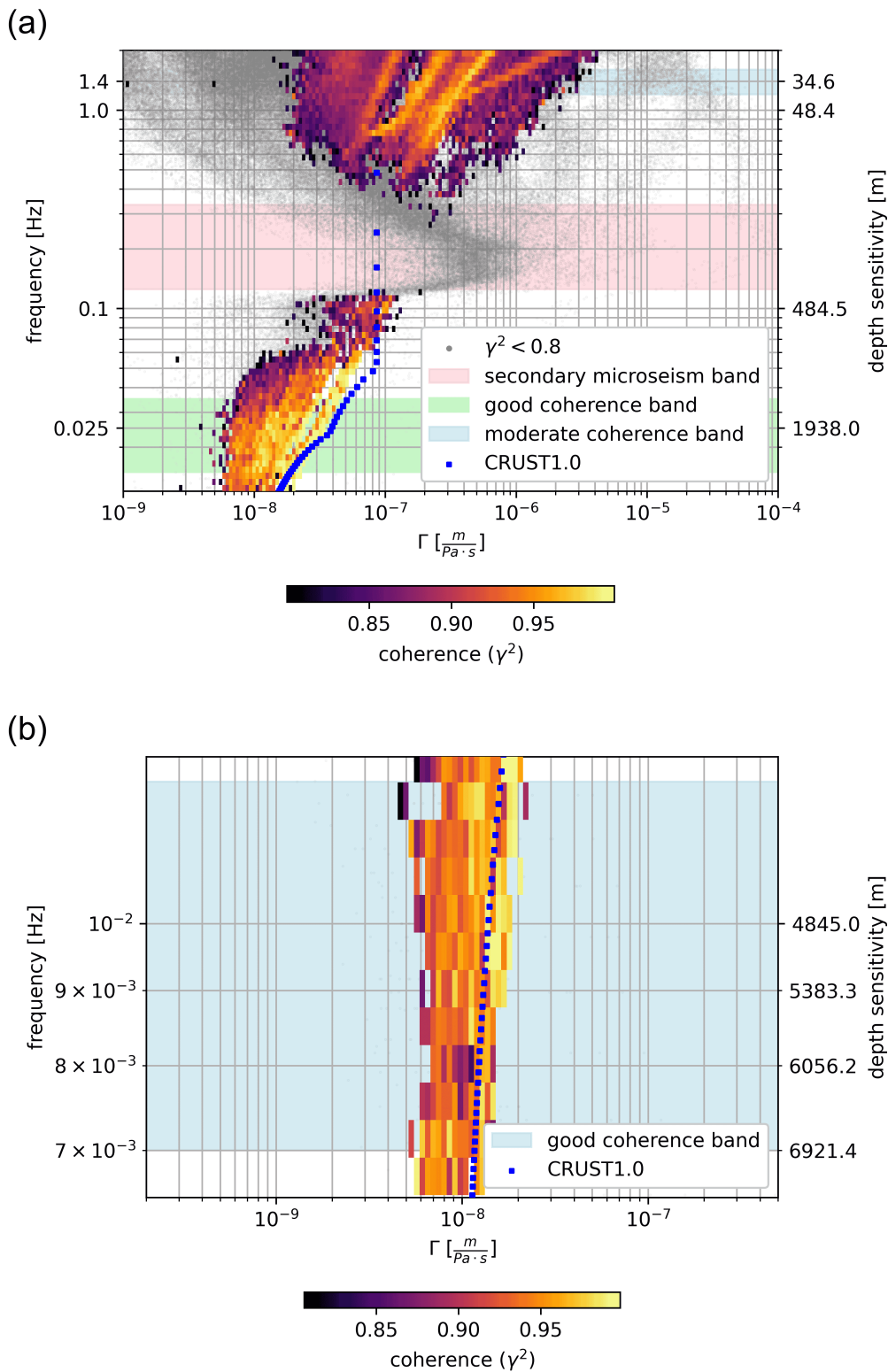


**Figure 4** (a) Coupling spectra from 0.01 to 2.0 Hz. The pressure data used at these frequencies are from infrasound sensors. (b) Coupling spectra from 0.0065 to 0.013 Hz. The pressure data at these frequencies were recorded on barometers. The horizontal axes are the coupling ratio from equation 3 and the vertical axes are frequency. For coupling values with high coherence ( $\geq 0.8$ ) amplitudes are colored by coherence. Low coherence values are denoted by small gray dots. The depth sensitivity corresponding to the frequencies from equation 2 are shown on the right vertical axes. The microseism band and target bands of good or moderate coherence are shown by red, green, and blue boxes, respectively. Theoretical coupling values from equation 5 with depth-averaged material parameters from the CRUST1.0 model are shown by blue squares.

from HTHH that were recorded in the Alaska region. These predictions include that coupling amplitude is in-

versely proportional to the rigidity of the material (we rely on this for our  $V_s$  estimates); vertical seismic veloc-

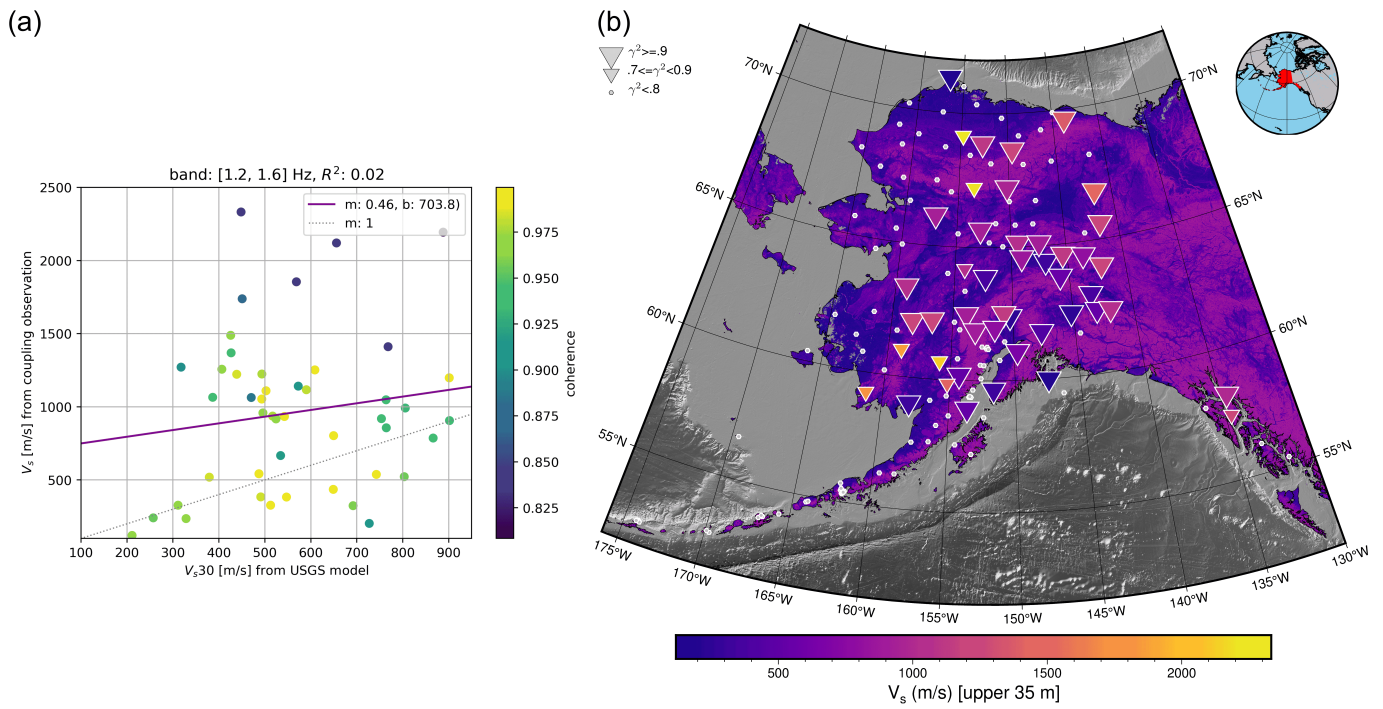


**Figure 5** Results of calculating  $V_s$  from coupling in the 1.2 to 1.6 Hz band, corresponding to a mean depth of 35 m. (a) Scatter plot of mean  $V_s$  to a depth of 35 m estimated from coupling as a function of  $V_{s30}$  from the USGS global map ( $V_{s30}Model$ ), with symbols colored by coherence. The purple line is the best-fit line with the  $R^2$  value indicated at the top. The dotted line has slope of 1 and vertical-intercept of 0. (b) Spatial view with stations plotted as inverted triangles scaled by coherence and colored by the  $V_s$  to a depth of 35 m estimate from coupling. The background map is the  $V_{s30}Model$ , and uses the same color bar that is used to color the stations.

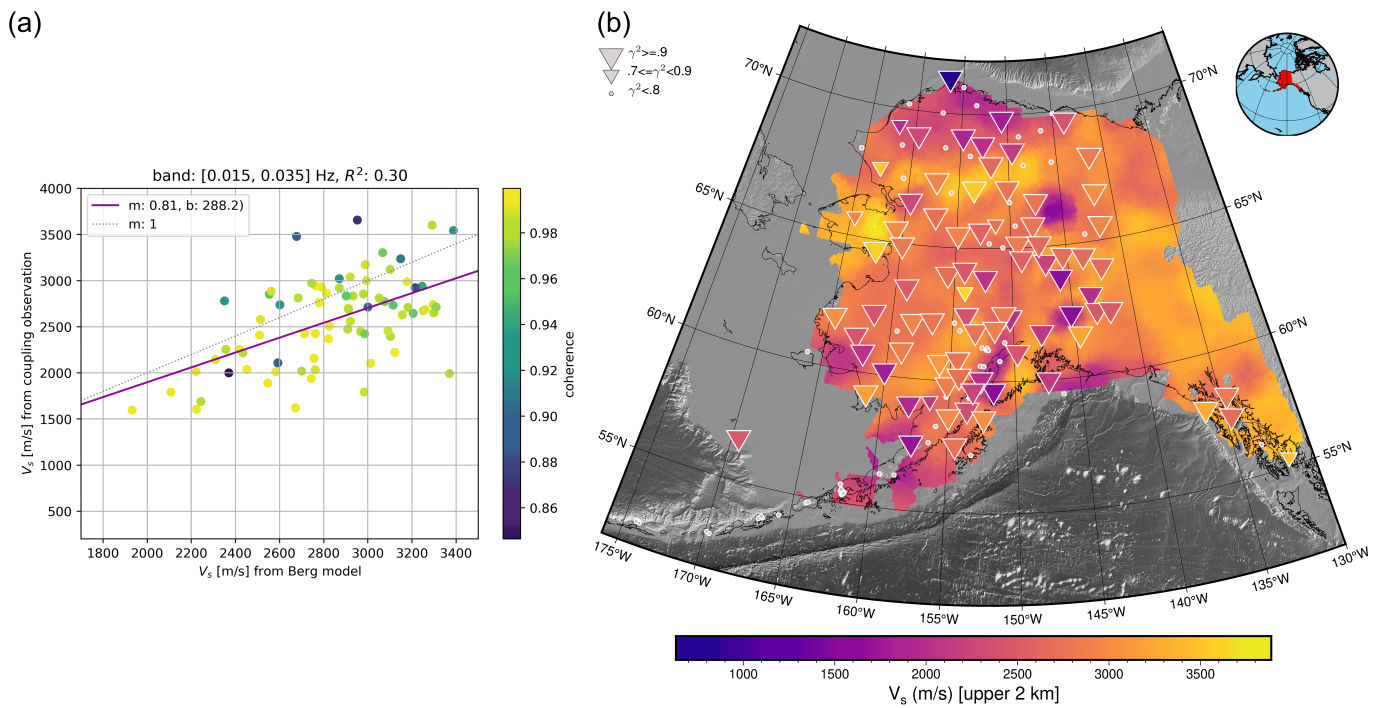


**Figure 6** Results of calculating  $V_s$  from coupling in the 0.015 to 0.035 Hz band, corresponding to a mean depth of 2 km. (a) Scatter plot of mean  $V_s$  to a depth of 2 km estimated from coupling as a function of  $V_s$  from the Berg et al. (2020) tomographic model depth-averaged to 2 km, with symbols colored by coherence. The purple line is the best-fit line with the  $R^2$  value indicated at the top. The dotted line has slope of 1 and vertical-intercept of 0. (b) Spatial view with stations plotted as inverted triangles scaled by coherence and colored by  $V_s$  to a depth of 2 km estimate from coupling. The background map is the Berg model depth-averaged to a depth of 2 km, and uses the same color range.

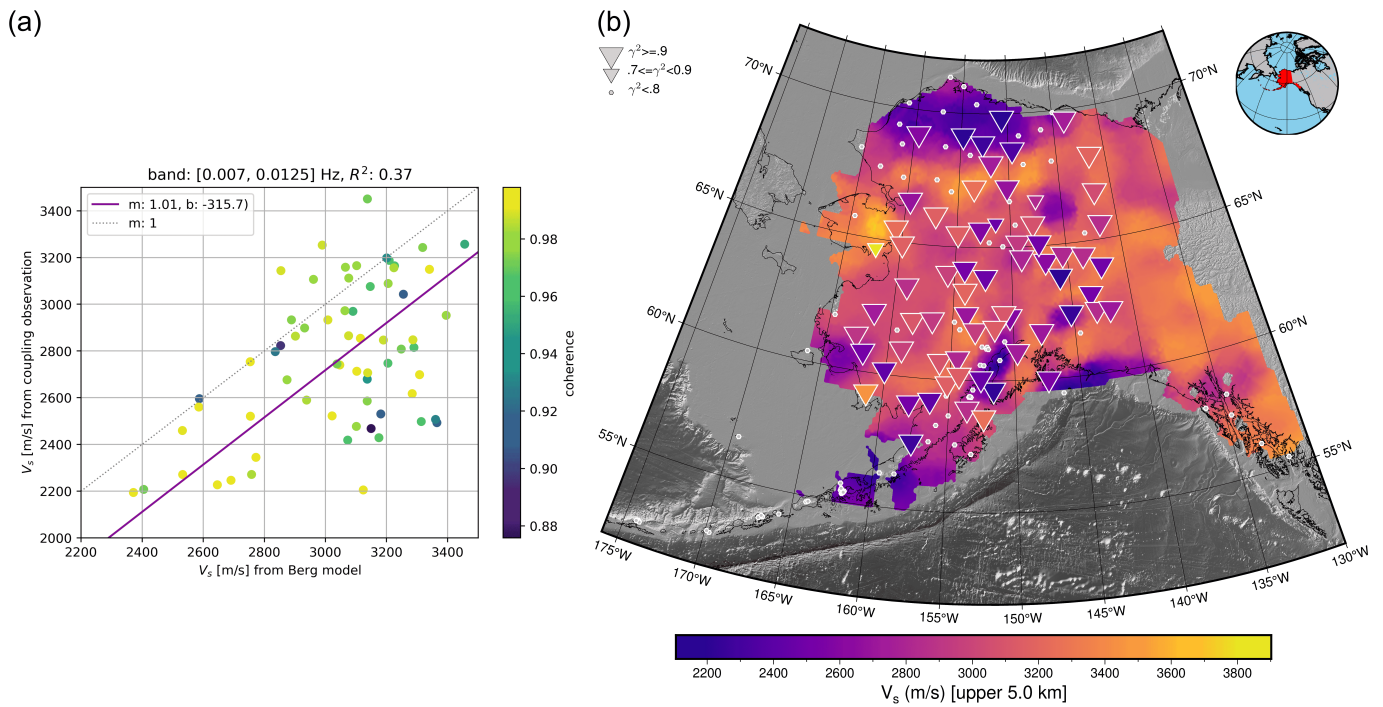


**Figure 7** Results of calculating  $V_s$  from coupling in the 0.007 to 0.0125 Hz band, corresponding to a mean depth of 5 km. (a) Scatter plot of mean  $V_s$  to a depth of 5 km estimated from coupling as a function of  $V_s$  depth-averaged to 5 km from the Berg et al. (2020) tomographic model, with symbols colored by coherence. The purple line is the best fit line with the  $R^2$  value indicated at the top. The dotted line has slope of 1 and vertical-intercept of 0. (b) Spatial view with stations plotted as inverted triangles scaled by coherence and colored by the  $V_s$  to a depth of 5 km estimate from coupling. The background map is the Berg model depth-averaged to 5 km, and uses the same color range.

ity should be correlated with the 90° phase-delayed pressure record; radial seismic velocity will be correlated with the pressure record, indicating retrograde particle motion; radial velocity amplitudes should be around half of the vertical velocity amplitude; and seismic velocity amplitudes will vanish on the tangential component (Matoza and Fee, 2014; Anthony et al., 2022b,a; Bishop et al., 2023). We investigated these predictions by examining all three components of ground motion excited by the HTHH pressure wave. We assumed a source location for the HTHH eruption of 175.39°W, 20.546°S as reported by U.S. Geological Survey Earthquakes Hazards Program (2017) to rotate the horizontal components into a radial-tangential orientation, and we note many discrepancies between the theory and our observations. For example, we show HTHH waveforms in Figure 8a, recorded at station M26K in central Alaska (see Fig. 1) that violate several of the conditions that we expect from theory. The vertical, radial, and tangential velocity waveforms are shown in the top three panels, respectively, along with the pressure record. Seismic and infrasound PSDs and coherence are shown in the lower panel. All waveforms have been filtered between 0.015 and 0.035 Hz. We observe good coherence near 0.025 Hz for this station, as we generally do for the network, and also good high-frequency coherence. In the top panel showing the vertical velocity and pressure, the pressure record has been phase delayed by 90° via a Hilbert transform. We show zoomed-in details of the time domain plots of four minutes of data in Figure 8b, with the background color of each panel corresponding

to the region indicated by shading in 8a. Note that the top two panels of 8b both show a comparison of vertical seismic velocity and infrasound, but that the infrasound has been phase-delayed by 90° via a Hilbert transform in the lower panel. We have cross-correlated the pressure waveforms with the velocity waveforms for both the vertical and radial components without time shifts, and the correlation coefficients are noted at the top of the plot. We observe that the phase-delayed pressure is highly correlated with the vertical velocity, with a correlation of  $\approx 0.99$  as predicted by theory. However, unexpectedly, we observe that the radial component of velocity is out of phase with the non-phase-delayed pressure record, with a correlation value of  $\approx -0.04$ , indicating prograde particle motion. Further, velocity amplitudes of the radial component are actually larger than the vertical component, and we observe significant energy in the tangential component. These observations indicate that some of the assumptions included in the theory of Sorrells (1971) are not valid for the coupled waves from HTHH eruption recorded at M26K. In fact, these features are widespread for HTHH observations on the regional network. Of the 82 stations with high coherence in the 0.015 to 0.025 Hz passband, all have correlation coefficients between phase-delayed pressure and vertical velocity above 0.7, with a mean correlation of 0.96, while 43 stations have correlation coefficients between pressure and radial velocity below 0.7, with a mean correlation of 0.49. This is similar to the low radial correlations observed by Anthony et al. (2022a) in their study of HTHH waveforms on the GSN. There are also 68 sta-

tions where the maximum amplitude on the radial velocity component is in excess of half of the maximum amplitude on the vertical component. To determine if these observations are a result of uncertainty in source location or path effects, we performed a grid search between  $0^\circ$  and  $360^\circ$  to find the back azimuth that minimized the tangential velocity amplitude, but did not observe an improvement in the number of stations with low radial correlations (Bishop et al., 2023). However, it remains plausible that this simple test does not capture the effect of different multi-pathed arrivals from this distant source on the observed complexity.

Another possible explanation for the lack of correlation between radial components and pressure at many stations, and one suggested by Anthony et al. (2022a) in their study of the GSN, is that the seismic horizontal components are contaminated by tilt noise. In their study, Anthony et al. (2022a) noted that the only GSN stations exhibiting high correlations between radial seismic and pressure were at deep borehole sites that are likely to be less susceptible to tilt. Tilt would also explain the apparent random distribution of low-correlation stations across the region that we observe, as it has been shown that tilt susceptibility is a function of highly local site conditions that can operate at scales of less than 10 m (Alejandro et al., 2020). We show in Figure 9, that while high vertical correlations are observed over the entire study region (Fig.9a), stations with poor radial correlation appear to be somewhat randomly distributed (Fig.9b), and this indicates that complex site conditions might be inducing tilt at some station but not at others. To explore this possibility, we examine HTHH waveforms at the GSN station COLA, in interior Alaska (see Fig. 1). This station is equipped with a broadband seismometer at the surface, a broadband seismometer in a 117 m deep borehole, and a Setra barometer. We show waveform details in the 0.015 to 0.035 Hz pass-band from station COLA, with Figure 9c showing radial seismic from the seismometer at the surface and Figure 9d showing radial seismic from the borehole seismometer. While both locations show high vertical correlation between the pressure and vertical seismic, only the deep sensor shows high radial coherence. This supports the theory that many of the stations exhibiting low radial correlations are being affected by tilt contamination. If this is indeed the case, the variability of the degree of tilt susceptibility across the network is remarkable, as these are former TA sites with very similar 2-3 m posthole installations (Busby and Aderhold, 2020). Another possibility is that low  $V_s$  at soft-soil sites or shallow seismic velocity inversions may be inducing prograde motion resulting in low radial correlation. To investigate this, we plotted the pressure-radial cross-correlation as a function of our  $V_s$  estimate (see Fig. 10a). The figure indicates that there is no clear relationship between  $V_s$  and radial channel correlation values. While this evidence indicates that tilt contamination on horizontal channels is most likely causing the low infrasound-radial correlation, more work is required to show this definitively.

The simplification of equation 5 derived by Wang and Tanimoto (2020) that we follow in this study is required

because there are two unknown Lamé parameters,  $\lambda$  and  $\mu$ , in a single coupling equation. However, Sorrells (1971) also provides the following equation for the response of the half space in terms of the seismic-to-pressure ratio from the radial component of a seismometer,

$$\bar{\Gamma}_{radial} = \frac{c}{2(\lambda + \mu)}. \quad (9)$$

By using this expression along with equation 5, it is theoretically possible to solve for the Lamé parameters directly, without the need to neglect  $\lambda$ . We initially adopted this approach, but due to the high number of stations with large radial amplitudes relative to the vertical amplitudes, equation 9 was of limited use, so we abandoned this approach. As discussed above, the horizontal components of many stations are likely contaminated by tilt noise, making them unsuitable for use with equation 9. While it may be possible to use horizontal channels for higher-frequency analysis, where tilt is negligible, we reiterate that the simplification derived by Wang and Tanimoto (2020) that we follow here is simple, effective, and supported by the prediction that seismic amplitude be inversely proportional to material rigidity.

## 4.2 Limitations

It should be noted that the velocity estimates from this study are mean velocities from the surface to the respective depths, rather than velocity profiles. In order to develop profiles of layer velocities, the inversion method of Tanimoto and Wang (2019) could be employed, or a joint inversion scheme using an additional data set such as seismic receiver functions. However, simple mean velocities are useful for applications such as crustal corrections for tomography or individual station corrections for routine earthquake location, and of course, the mean velocity to a depth of 30 m is applicable for seismic hazard assessment. Further, the method here avoids the complexity of inversion schemes that are typically ill-posed with non-unique solutions (Rawlinson et al., 2014).

Another limitation of our results is the lack of a relationship between our  $V_s$  estimates to a depth of 30 m and  $V_{s30}$  (see Fig. 5). Although our values appear realistic overall for near-surface  $V_s$ , they are generally slower than the  $V_{s30}$  values, and are not linearly related ( $R^2$  is essentially zero). In order to test if the discrepancies are dependent on topography, we investigated the percent difference between our velocity estimates and model estimates as a function of station elevation (see Fig. 10b) but observed no clear relationship, with the exception that the largest differences occur for the shallow estimates. The poor relationship between our estimates and the proxy  $V_{s30}$  is similar to what was observed by Wang and Tanimoto (2020) for Alaska, using coupling from wind as the pressure source to estimate  $V_{s30}$ , with many values in Alaska being above 900 m/s, the maximum value of the  $V_{s30}Model$ . Those authors surmised that permafrost in Alaska may result in high velocities at stations on flat terrain, indicating a limi-

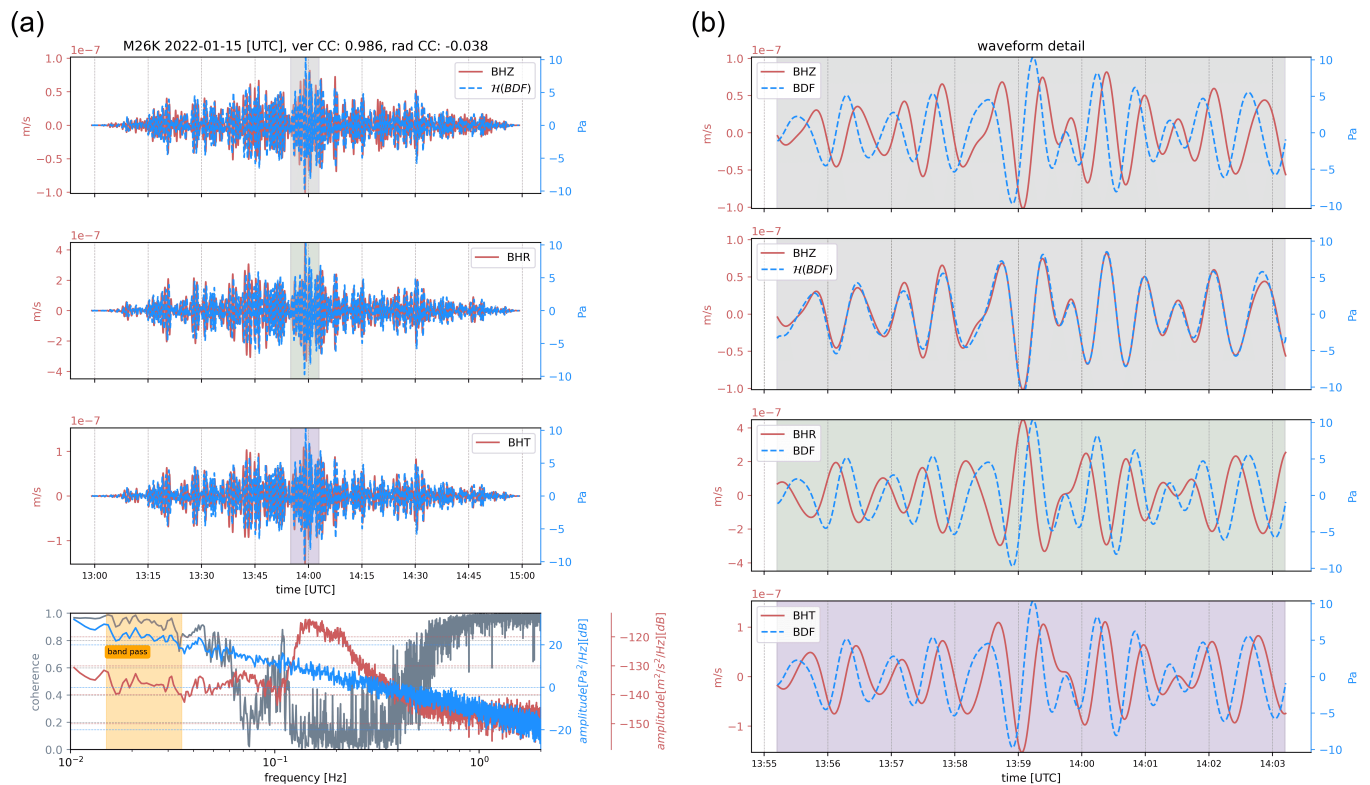


**Figure 8** Waveforms, spectra, and coherence from the HTHH eruption recorded at station M26K. All waveforms have been bandpass filtered between 0.015 and 0.035 Hz. (a) Two hours of data with infrasound plotted as dotted blue lines and seismic velocity plotted as solid red. The top three panels show vertical velocity, radial velocity, and tangential velocity, respectively. The infrasound record in the top panel has been phase-delayed by  $90^\circ$  by applying a Hilbert transform. Correlation coefficients for the cross-correlation between the phase-delayed infrasound and the vertical velocity and between the infrasound (not phase delayed) and the radial velocity are noted at the top. The bottom panel shows the seismic velocity PSD in red, the infrasound PSD in blue, and the coherence in gray. The bandpass region is denoted by an orange box in the bottom panel. Colored regions in the time domain indicate the segment that is shown in detail on the right. (b) Zoomed-in detail of four minutes of data from (a). Panel background colors indicates correspondence with the longer duration waveforms in (a). Note that the top panel compares the vertical velocity with infrasound, while the second panel shows the same but with a  $90^\circ$  phase delay imposed on the infrasound.

tation in the proxy  $V_{s30}$  method for far northern stations. To further investigate this, we show the percent difference between our shallow  $V_s$  estimates and the  $V_{s30}Model$  plotted as a function of topographic slope in Figure 10c, with symbols colored by our  $V_s$  estimate. Although there is a lack of a linear relationship ( $R^2 \approx 0$ ), the figure does show the most scatter for stations in flatter topography. In fact, if we drop stations for which our  $V_s$  estimates exceed the maximum  $V_{s30}Model$  value of 900 m/s and re-plot Figure 5a, much of the scatter disappears, and we achieve a modest linear relationship ( $R^2 = 0.38$ ) for 21 stations, as can be seen in Figure 10d. Other studies have shown considerable scatter when comparing proxy  $V_{s30}$  values to ground truth. For example, Lemoine et al. (2012) found that the proxy method only outperformed blind chance for hard rock sites when comparing with ground-truth data in Europe, and recommended that the method not be used for sites with any geological complexity, such as small basins, flat hard-rock sites, or coastal sites. Given the diversity of geological conditions encompassed by the Alaska seismoacoustic network, the absence of a relationship between our observations and the proxy values

is not surprising.

### 4.3 Comparison with coupling from the Chelyabinsk bolide

The fact that the HTHH eruption is unprecedented in the instrumental age is both fortuitous and a limitation. The limitation is that our estimation of  $V_s$  relies on a single observation at each station. To enhance confidence in our method and results, we sought long-period infrasound sources in the region that occurred during the operation of the seismoacoustic network. The Chelyabinsk bolide was a result of atmospheric entry of a small asteroid over Russia, and generated infrasound that was recorded over a wide region, including by a few experimental TA-like stations in Alaska (de Groot-Hedlin and Hedlin, 2014). At the time of the asteroid entry, February 15th, 2013, the TA was only operating two test stations in Alaska: TOLK and POKR (see Fig. 1), which are previously existing stations that were upgraded with TA equipment, including infrasound sensors. Infrasound generation from bolides is complex, as it is generated by a non-linear shock wave as the object interacts with the atmosphere at hypersonic veloci-

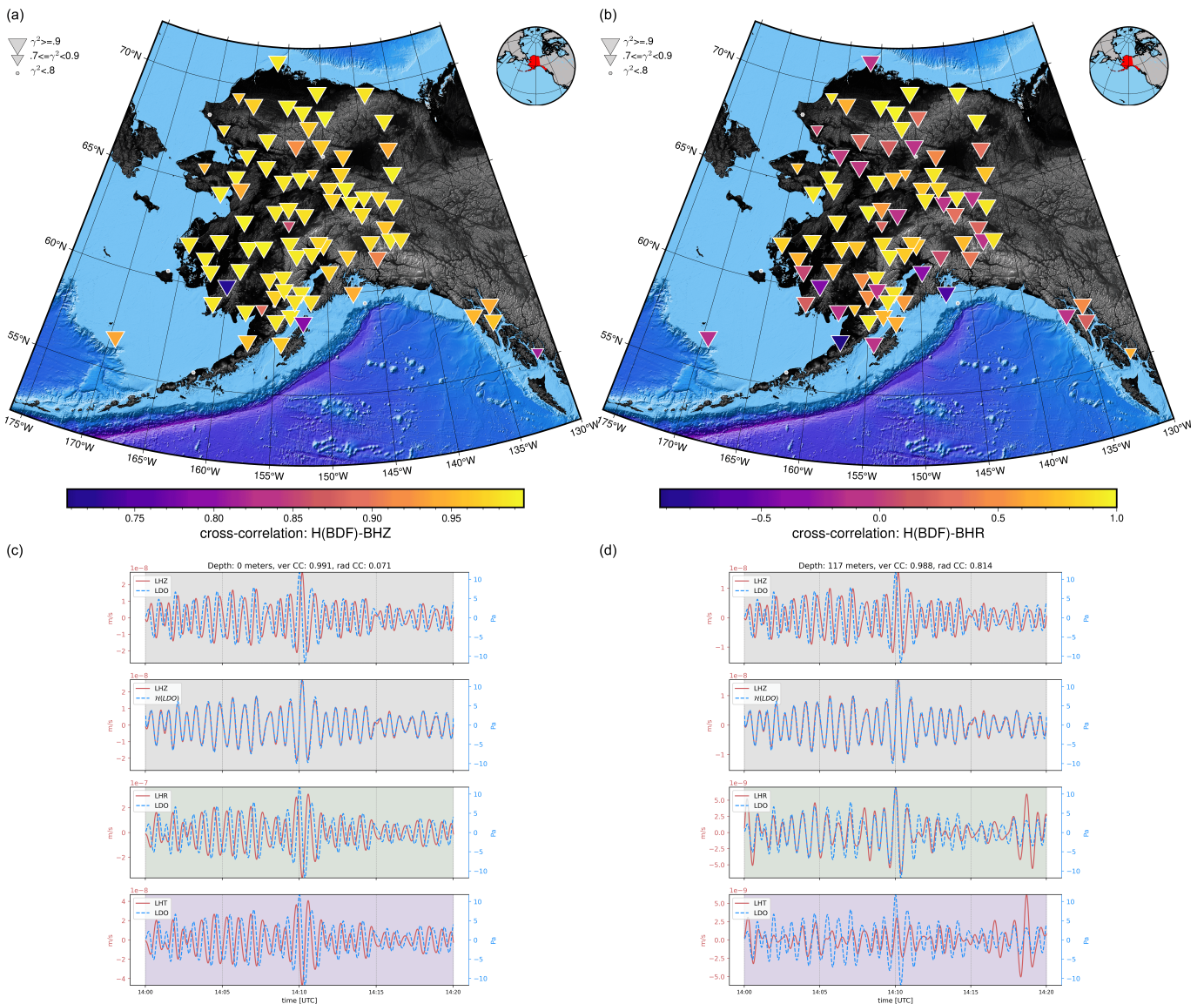


**Figure 9** (a) Map view of cross correlation values between the phase-delayed infrasound and vertical seismic recordings in the 0.015 to 0.035 Hz passband. (b) Map view of cross correlation values between the infrasound and radial seismic recordings in the 0.015 to 0.035 Hz passband. (c) Detail of four minutes of data from station COLA, filtered between 0.015 and 0.035 Hz. The seismic from the surface seismometer is shown in red, while the pressure record from the colocated barometer is plotted in blue, and the cross correlations between vertical seismic and phase-delayed pressure and for radial seismic and pressure for 2 hours of data is indicated at the top. (d) Same as in (c), but the seismic data is from the borehole seismometer at a depth of 117 m. Note that in the second panel of (c) and (d), the pressure has been phase-delayed.

ties (Edwards, 2009). However, at large offsets the infrasound propagates as a plane wave at acoustic velocities, and IMS array detections of the Chelyabinsk infrasound confirm this (Le Pichon et al., 2013). Stations TOLK and POKR are approximately 6,000 km and 6,400 km from the location of maximum brightness, where the asteroid likely broke up. Because the bolide-generated infrasound was likely plane waves traveling at acoustic velocities when they reached TOLK and POKR, we can use this source to estimate seismic velocities beneath the stations.

We show waveforms and spectra from the bolide recorded at station TOLK in Figure 11. Waveforms are filtered between 0.015 and 0.035 Hz, and spectra show good coherence in this band, supporting the observation of the dependence of strong coupling on ambi-

ent seismic noise. Similar to the HTHH waveforms at M26K, the Chelyabinsk waveforms at TOLK exhibit high correlation between the phase-delayed pressure and the vertical velocity, poor correlation between pressure and the radial component, and significant tangential velocity energy. We apply our method to estimate mean  $V_s$  to a depth of 2 km beneath stations POKR and TOLK using the Chelyabinsk coupled waveforms and compare the results with our HTHH estimates. For station POKR, we get a value of 2,645 m/s from Chelyabinsk, and 2,630 m/s from HTHH, a discrepancy of less than 1%. For station TOLK, we find 2,156 m/s from Chelyabinsk and 2,158 m/s for HTHH, a discrepancy of much less than 1%. For the higher-frequency passband corresponding to a depth of 35 m, the mean coherence in the band is too low for POKR to permit a  $V_s$  calculation ( $\gamma^2 < 0.5$ ), and

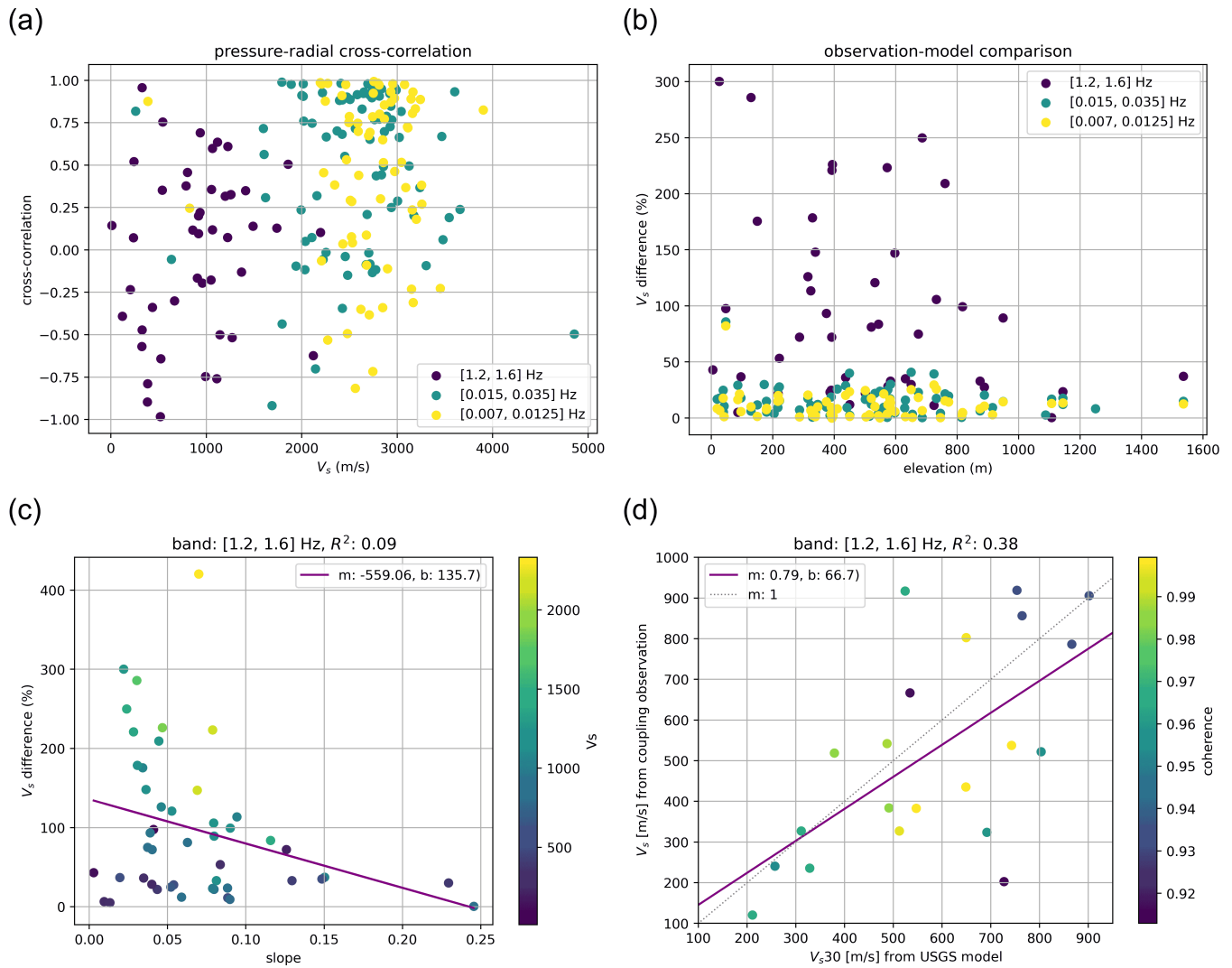


**Figure 10** (a) Scatter plot of the cross-correlation between the pressure and radial seismic waveforms plotted as a function of  $V_s$  estimate. The dots are colored by the passband. (b) Scatter plot of percent difference between  $V_s$  estimate from coupling and model estimate for each station as a function of station elevation. The dots are colored by the passband. (c) Percent difference between  $V_s$  estimate for 35 m and USGS  $V_{s30}$  map values ( $V_{s30} Model$ ) as a function of topographic slope. Symbols are colored by the  $V_s$  estimate for 35 meters. (d) Replot of Figure 5a but only plotting stations with  $V_s \leq 900$  m/s. Symbols are colored by coherence.

is marginal for TOLK ( $\gamma^2 = 0.76$ ). In this band for station TOLK, we get a  $V_s$  value of 1,112 m/s from Chelyabinsk and 1,257 m/s from HTHH, or about a 12% difference. We suspect this moderate difference is a result of the relatively poor high-frequency coupling at the station from the Chelyabinsk event. While ideally we would make such comparisons for multiple sources and all stations in the network, sources that generate low-frequency infrasound over large geographic regions are exceedingly rare. However, we feel that the close agreement of  $V_s$  estimates at these two stations using very different infrasound sources provides a degree of confidence in our approach.

## 5 Conclusions

We have leveraged a regional network of seismoacoustic stations in Alaska along with pressure waves from the January 2022 HTHH eruption, a source unprecedented

in the instrumental age, to estimate mean crustal velocities at three depths beneath the seismoacoustic network. Using a simple expression that relates frequency to coupling depth-sensitivity (eq. 2) in three separate pass bands of 1.2 to 1.6 Hz (0.83 to 0.63 sec), 0.015 to 0.035 Hz (66.6 to 28.6 sec), and 0.007 to 0.0125 Hz (142.85 to 80.00 sec), we are able to compute mean  $V_s$  to depths of 35 m, 2 km, and 5 km. Our results produce a reasonable range of  $V_s$  for these depths, but do not correlate well with  $V_{s30}$  values from the  $V_{s30} Model$  global map. This is likely due to the fact that  $V_{s30} Model$  estimates in Alaska are predominantly derived from proxy values, and it has been shown that direct observations often differ from these values (Lemoine et al., 2012). Our mean upper crustal  $V_s$  estimates to 2 km and 5 km generally agree with the depth-averaged values from the tomographic model of Berg et al. (2020). Our estimates show generally realistic velocities for the depths considered, and reveal features such as low-velocity zones associ-

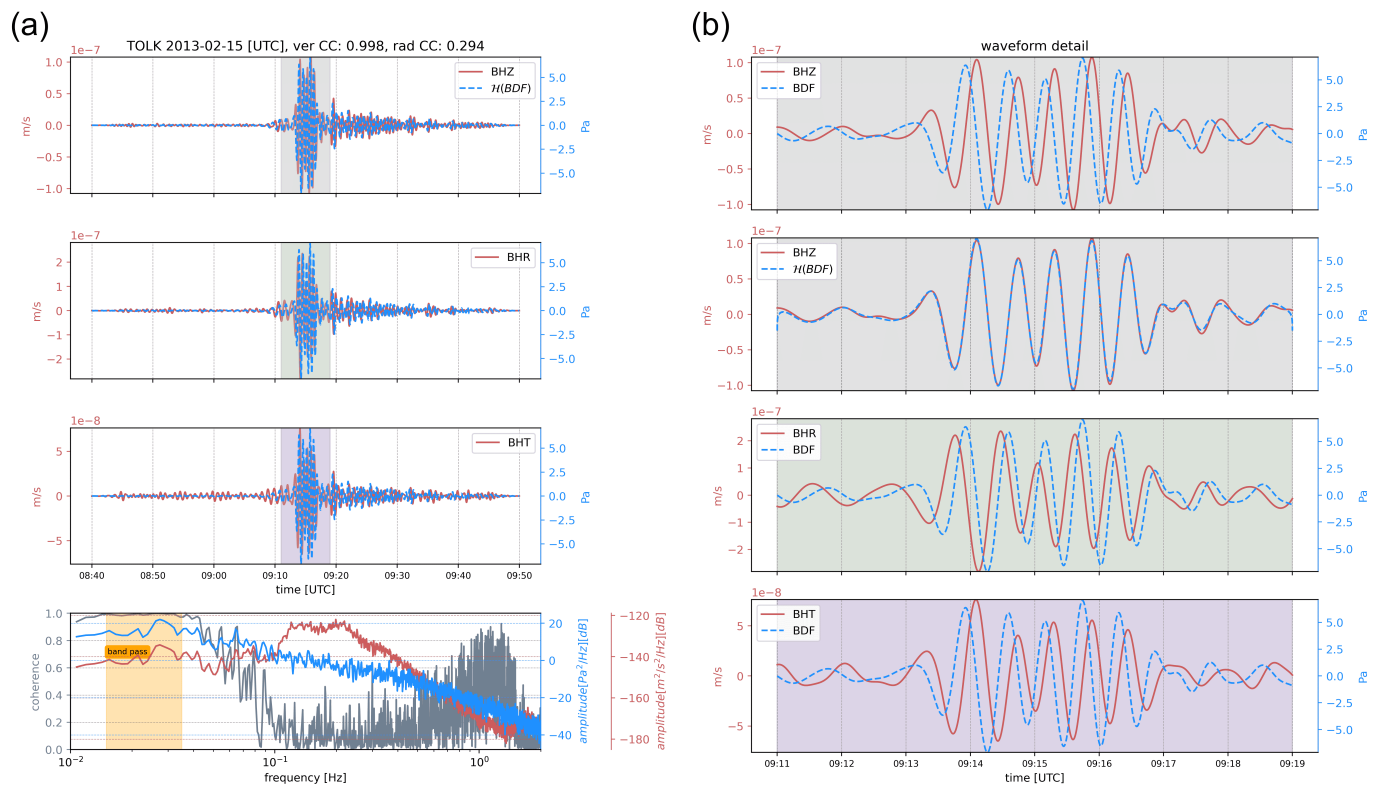


**Figure 11** Waveforms, spectra, and coherence from the Chelyabinsk bolide recorded at station TOLK. All waveforms have been bandpass filtered between 0.015 and 0.035 Hz. (a) 2 hours of data with infrasound plotted as dotted blue lines and seismic velocity plotted as solid red. The top three panels show vertical velocity, radial velocity, and tangential velocity, respectively. The infrasound record in the top panel has been phase-delayed by  $90^\circ$  by applying a Hilbert transform. Correlation coefficients for the cross-correlation between the phase-delayed infrasound and the vertical velocity and between the infrasound (not phase delayed) and the radial velocity are noted at the top. The bottom panel shows the seismic velocity PSD in red, the infrasound PSD in blue, and the coherence in gray. The bandpass region is denoted by an orange box in the bottom panel. Colored regions in the time domain indicate the segment that is shown in detail on the right. (b) Zoomed-in detail of four minutes of data from (a). Panel background colors indicates correspondence with the longer duration waveforms in (a). Note that the top panel compares the vertical velocity with infrasound, while the second panels shows the same but with a  $90^\circ$  phase delay imposed on the infrasound.

ated with the North Slope basin and Cook Inlet basin.

Coupled seismic waves from this event exhibit complexity that is not predicted by the theory of Sorrells (1971) or Ben-Menahem and Singh (1981). In particular, we observe on three component seismometers significant tangential energy and radial amplitudes in excess of vertical amplitudes, in agreement with work by Wills et al. (2022) and Anthony et al. (2022b). Also, while vertical velocity is highly correlated for all stations with  $90^\circ$  phase-shifted pressure, many stations exhibit poor correlations between radial velocity and pressure that has not been phase shifted. Because stations with poor radial-pressure coherence are spatially distributed randomly, the mostly likely explanation for this is that some horizontal channels are contaminated by tilt noise. The fact that a station with a surface seismometer and a borehole seismometer shows poor correlation for the shallow instrument and good correlation for the deep instrument further supports the tilt hypothesis, as tilt signal is known to attenuate rapidly with depth (Sorrells, 1971). Compromised horizontal recordings support our use of the simplified theory of Wang and Tanimoto (2020) that we employ via equation 7 to estimate

$V_s$ .

The velocity estimates presented above are from simple, direct observations and do not require inversion, with the uncertainties and potentially ill-posed nature of the schemes associated with that strategy. The fact that a pressure source with source-receiver offsets on the order of 10,000 km excited the crust to a depth of at least 5 km is remarkable (Anthony et al., 2022a). We have used this unique source to compute  $V_s$  from coupling to a depth that has not, to our knowledge, been previously accomplished. The velocity values computed in this study may be useful for ground-motion modeling, station corrections in regional earthquake solutions, or crustal corrections for tomographic studies. Further study of the air-to-ground coupled HTHH waveforms in the Alaska region may lead to an enhanced understanding of the deviation of observations from the theory of Sorrells (1971), Ben-Menahem and Singh (1981), and Tanimoto (2024). In particular, understanding why some stations exhibit seismic waveforms with the expected retrograde motion while others do not, and how this relates to frequency content and site conditions, promises to be a fruitful avenue of study.

## Acknowledgements

The authors acknowledge the Alaska Native nations upon whose land our study area resides and note the stewardship of the traditional inhabitants of the region. This research was supported by the Defense Threat Reduction Agency Nuclear Arms Control Technology program under Contract Numbers HQ003421F0112 and HD-TRA121C0030 (Distribution statement: Cleared for release); any use of trade, firm, or product names is for descriptive purposes only and does not imply endorsement by the authors, their institutions, or the U.S. Government. The authors would like to thank two external reviewers, Ronan LeBras at the Comprehensive Test Ban Treaty Organization and Toshiro Tanimoto at the University of California Santa Barbara, who provided valuable comments that improved the final manuscript. We thank the Seismica editor, György Hetényi, for helpful comments and suggestions that improved the manuscript. We also thank three internal reviewers, Alexandra Iezzi and Michelle Coombs of the U.S. Geological Survey, and Karen Pearson of the Defense Threat Reduction Agency, for helpful feedback that improved the article. The authors thank members of the Wilson Alaska Technical Center for always helpful discussions in preparation of this article.

## Data and code availability

All pressure and seismic data used in this study were produced by the networks of the Alaska Earthquake Center (AK, [Alaska Earthquake Center, Univ. of Alaska Fairbanks, 1987](#)), the Alaska Volcano Observatory (AV, [Alaska Volcano Observatory/USGS, 1988](#)), and the Global Seismographic Network (GSN, [Scripps Institution of Oceanography, 1986](#)), and these data are available from the Seismological Facility for the Advancement of Geoscience Data Management Center (SAGE DMC; <http://ds.iris.edu/ds/nodes/dmc/>, last accessed July 2024). We used Python code developed by Adam Ringler at the USGS and available at [https://github.com/aringle-usgs/Tonga\\_SA](https://github.com/aringle-usgs/Tonga_SA) (last accessed July, 2024) to read the CRUST1.0 model. The USGS Global  $V_{s30}$  map is available at <https://www.usgs.gov/programs/earthquake-hazards/science/vs30-models-and-data> (last accessed December 2024) and the Alaska shear-wave velocity model from [Berg et al. \(2020\)](#) is available at [https://ds.iris.edu/ds/products/emc-alaskajointinversion\\_rfvphv-1berg2020/](https://ds.iris.edu/ds/products/emc-alaskajointinversion_rfvphv-1berg2020/) (last accessed December 2025). The CRUST1.0 velocity model is available at <https://ds.iris.edu/ds/products/emc-crust10/> (last accessed June 2024). Our results are available in a supplemental CSV file that includes coupling ratios, max peak-to-peak pressure, rigidity, and  $V_s$  by pass-band for each station with high coherence. This project relied heavily on free and open-source software packages including ObsPy ([The ObsPy Development Team, 2020](#)) and PyGMT ([Uieda et al., 2021](#)).

## Competing interests

The authors acknowledge that there are no conflicts of interest recorded.

## References

- Aki, K. and Richards, P. G. *Quantitative seismology*. Cambridge University Press, 2002.
- Alaska Earthquake Center, Univ. of Alaska Fairbanks. Alaska Regional Network [dataset], 1987. doi: 10.7914/SN/AK.
- Alaska Volcano Observatory/USGS. Alaska Volcano Observatory [dataset], 1988. doi: 10.7914/SN/AV.
- Alejandro, A. C. B., Ringler, A. T., Wilson, D. C., Anthony, R. E., and Moore, S. V. Towards understanding relationships between atmospheric pressure variations and long-period horizontal seismic data: a case study. *Geophysical Journal International*, 223(1):676–691, 07 2020. doi: 10.1093/gji/ggaa340.
- Anglin, F. M. and Haddon, R. A. W. Meteoroid Sonic Shock-Wave-Generated Seismic Signals Observed at a Seismic Array. *Nature*, 328(6131):607–609, Aug. 1987. doi: 10.1038/328607a0.
- Anthony, R. E., Ringler, A. T., Tanimoto, T., Matoza, R. S., De Angelis, S., and Wilson, D. C. Earth’s Upper Crust Seismically Excited by Infrasonic from the 2022 Hunga Tonga–Hunga Ha’apai Eruption, Tonga. *Seismological Research Letters*, Dec. 2022a. doi: 10.1785/0220220252.
- Anthony, R. E., Watzak, J., Ringler, A. T., and Wilson, D. C. Characteristics, relationships and precision of direct acoustic-to-seismic coupling measurements from local explosions. *Geophysical Journal International*, 230(3):2019–2035, 04 2022b. doi: 10.1093/gji/ggac154.
- Beauduin, R., Lognonné, P., Montagner, J. P., Cacho, S., Karczewski, J. F., and Morand, M. The Effects of the Atmospheric Pressure Changes on Seismic Signals or How to Improve the Quality of a Station. *Bulletin of the Seismological Society of America*, 86(6):1760–1769, Dec. 1996. doi: 10.1785/BSSA0860061760.
- Ben-Menahem, A. and Singh, S. J. *Seismic waves and sources*. Springer Science & Business Media, 1981.
- Berg, E. M., Lin, F.-C., Allam, A., Schulte-Pelkum, V., Ward, K. M., and Shen, W. Shear Velocity Model of Alaska Via Joint Inversion of Rayleigh Wave Ellipticity, Phase Velocities, and Receiver Functions Across the Alaska Transportable Array. *Journal of Geophysical Research: Solid Earth*, 125(2):e2019JB018582, Feb. 2020. doi: 10.1029/2019JB018582.
- Bishop, J. W., Haney, M. M., Fee, D., Matoza, R. S., McKee, K. F., and Lyons, J. J. Back-Azimuth Estimation of Air-to-Ground Coupled Infrasonic from Transverse Coherence Minimization. *The Seismic Record*, 3(4):249–258, 10 2023. doi: 10.1785/0320230023.
- Busby, R. W. and Aderhold, K. The Alaska Transportable Array: As Built. *Seismological Research Letters*, 91(6):3017–3027, Nov. 2020. doi: 10.1785/0220200154.
- de Groot-Hedlin, C. D. and Hedlin, M. A. H. Infrasonic Detection of the Chelyabinsk Meteor at the USArray. *Earth and Planetary Science Letters*, 402:337–345, Sept. 2014. doi: 10.1016/j.epsl.2014.01.031.
- Dugick, F. D., Koch, C., Berg, E., Arrowsmith, S., and Albert, S. A New Decade in Seismoacoustics. *Bulletin of the Seismological Society of America*, 113(4):1390–1423, Dec. 2023. doi: 10.1785/0120220157.
- Edwards, W. N. Meteor generated infrasonic: theory and observation. *Infrasonic monitoring for atmospheric studies*, pages 361–414, 2009.
- Fee, D., Haney, M., Matoza, R., Szuberla, C., Lyons, J., and

- Waythomas, C. Seismic Envelope-Based Detection and Location of Ground-Coupled Airwaves from Volcanoes in Alaska. *Bulletin of the Seismological Society of America*, 106(3):1024–1035, 04 2016. doi: 10.1785/0120150244.
- Fuchs, F., Schneider, F. M., Kolínský, P., Serafin, S., and Bokelmann, G. Rich Observations of Local and Regional Infrasound Phases Made by the AlpArray Seismic Network after Refinery Explosion. *Scientific Reports*, 9(1):13027, Dec. 2019. doi: 10.1038/s41598-019-49494-2.
- Gabrielson, T. B. In Situ Calibration of Atmospheric-Infrasound Sensors Including the Effects of Wind-Noise-Reduction Pipe Systems. *The Journal of the Acoustical Society of America*, 130(3):1154–1163, 2011. doi: 10.1121/1.3613925.
- Heath, D. C., Wald, D. J., Worden, C. B., Thompson, E. M., and Smoczyk, G. M. A Global Hybrid VS30 Map with a Topographic Slope–Based Default and Regional Map Insets. *Earthquake Spectra*, 36(3):1570–1584, 2020. doi: 10.1177/8755293020911137.
- Hersbach, H., Bell, B., Berrisford, P., Biavati, G., Horányi, A., Muñoz Sabater, J., Nicolas, J., Peubey, C., Radu, R., Rozum, I., Schepers, D., Simmons, A., Soci, C., Dee, D., and Thépaut, J.-N. ERA5 hourly data on single levels from 1940 to present [dataset], 2023. doi: 10.24381/cds.adbb2d47.
- IRIS Transportable Array. USArray Transportable Array [dataset], 2003. doi: 10.7914/SN/TA.
- Kinsler, L. *Fundamentals of Acoustics*. John Wiley & Sons, 4 edition, 2000.
- Lamb, H. On the Vibrations of an Elastic Sphere. *Proceedings of the London Mathematical Society*, s1-13(1):189–212, 1881. doi: 10.1112/plms/s1-13.1.189.
- Langston, C. A. Seismic ground motions from a bolide shock wave. *Journal of Geophysical Research: Solid Earth*, 109(B12), 2004. doi: 10.1029/2004JB003167.
- Laske, G., Masters, G., Ma, Z., and Pasyanos, M. Update on CRUST1.0 - A 1-degree Global Model of Earth’s Crust. In *EGU General Assembly Conference Abstracts*, EGU General Assembly Conference Abstracts, pages EGU2013–2658, Apr. 2013.
- Le Pichon, A., Ceranna, L., Pilger, C., Mialle, P., Brown, D., Herry, P., and Brachet, N. The 2013 Russian fireball largest ever detected by CTBTO infrasound sensors. *Geophysical Research Letters*, 40(14):3732–3737, 2013. doi: 10.1002/grl.50619.
- Lemoine, A., Douglas, J., and Cotton, F. Testing the Applicability of Correlations between Topographic Slope and VS30 for Europe. *Bulletin of the Seismological Society of America*, 102(6): 2585–2599, 12 2012. doi: 10.1785/0120110240.
- Macpherson, K. A., Coffey, J. R., Witsil, A. J., Fee, D., Holtkamp, S., Dalton, S., McFarlin, H., and West, M. Ambient Infrasound Noise, Station Performance, and Their Relation to Land Cover across Alaska. *Seismological Research Letters*, page 20, 2022. doi: 10.1785/0220210365.
- Matoza, R. S. and Fee, D. Infrasonic component of volcano-seismic eruption tremor. *Geophysical Research Letters*, 41(6): 1964–1970, 2014. doi: 10.1002/2014GL059301.
- Matoza, R. S., Fee, D., Assink, J. D., Iezzi, A. M., Green, D. N., Kim, K., Toney, L., Lecocq, T., Krishnamoorthy, S., Lalande, J.-M., Nishida, K., Gee, K. L., Haney, M. M., Ortiz, H. D., Brissaud, Q., Martire, L., Rolland, L., Vergados, P., Nippres, A., Park, J., Shani-Kadmiel, S., Witsil, A., Arrowsmith, S., Caudron, C., Watada, S., Perttu, A. B., Taisne, B., Mialle, P., Le Pichon, A., Vergoz, J., Hupe, P., Blom, P. S., Waxler, R., De Angelis, S., Snively, J. B., Ringler, A. T., Anthony, R. E., Jolly, A. D., Kilgour, G., Averbuch, G., Ripepe, M., Ichihara, M., Arciniega-Ceballos, A., Astafyeva, E., Ceranna, L., Cevuard, S., Che, I.-Y., De Negri, R., Ebeling, C. W., Evers, L. G., Franco-Marin, L. E., Gabrielson, T. B., Hafner, K., Harrison, R. G., Komjathy, A., Lacanna, G., Lyons, J., Macpherson, K. A., Marchetti, E., McKee, K. F., Mellors, R. J., Mendo-Pérez, G., Miksell, T. D., Munaibari, E., Oyola-Merced, M., Park, I., Pilger, C., Ramos, C., Ruiz, M. C., Sabatini, R., Schwaiger, H. F., Tailpied, D., Talmadge, C., Vidot, J., Webster, J., and Wilson, D. C. Atmospheric Waves and Global Seismoacoustic Observations of the January 2022 Hunga Eruption, Tonga. *Science*, 377(6601): 95–100, July 2022. doi: 10.1126/science.abo7063.
- McKee, K., Fee, D., Haney, M., Matoza, R. S., and Lyons, J. Infrasound Signal Detection and Back Azimuth Estimation Using Ground-Coupled Airwaves on a Seismo-Acoustic Sensor Pair. *Journal of Geophysical Research: Solid Earth*, 123(8):6826–6844, 2018. doi: 10.1029/2017JB015132.
- McNamara, D. E. and Buland, R. P. Ambient Noise Levels in the Continental United States. *Bulletin of the Seismological Society of America*, 94(4):1517–1527, Aug. 2004. doi: 10.1785/012003001.
- Meltzer, A., Rudnick, R., Zeitler, P., Levander, A., Humphreys, G., Karlstrom, K., Ekstrom, G., Carlson, R., Dixon, T., Gurnis, M., Shearer, P., and van der Hilst, R. USArray Initiative. *GSA TODAY*, 9(11):40, 1999.
- Merchant, B. J. Hyperion 5113/GP Infrasound Sensor Evaluation. *The U.S. Department of Energy’s Office of Scientific and Technical Information*, 1(SAND-2015-7075), Aug. 2015. doi: 10.2172/1213302.
- Rawlinson, N., Fichtner, A., Sambridge, M., and Young, M. K. Chapter One - Seismic Tomography and the Assessment of Uncertainty. In Dmowska, R., editor, *Advances in Geophysics, Volume 55*, volume 55, pages 1–76. Elsevier, 2014. doi: 10.1016/bs.agph.2014.08.001.
- Ringler, A. T., Steim, J., Wilson, D. C., Widmer-Schmidrig, R., and Anthony, R. E. Improvements in seismic resolution and current limitations in the Global Seismographic Network. *Geophysical Journal International*, 220(1):508–521, 10 2019. doi: 10.1093/gji/ggz473.
- Sabatier, J. M., Bass, H. E., Bolen, L. N., and Attenborough, K. Acoustically induced seismic waves. *Journal of the Acoustical Society of America*, 80:646–649, 1986. doi: 10.1121/1.394058.
- Scripps Institution of Oceanography. Global Seismograph Network - IRIS/IDA [dataset], 1986. doi: 10.7914/SN/II.
- Shearer, P. M. *Introduction to Seismology*. Cambridge University Press, 3rd edition, 2019.
- Slater, J. A. and Malys, S. WGS 84 — Past, Present and Future. In Brunner, F. K., editor, *Advances in Positioning and Reference Frames*, pages 1–7, Berlin, Heidelberg, 1998. Springer Berlin Heidelberg.
- Sorrells, G. G. A Preliminary Investigation into the Relationship between Long-Period Seismic Noise and Local Fluctuations in the Atmospheric Pressure Field. *Geophysical Journal of the Royal Astronomical Society*, 26(1-4):71–82, Sept. 1971. doi: 10.1111/j.1365-246X.1971.tb03383.x.
- Tanimoto, T. Deformation of solid earth by surface pressure: equivalence between Ben-Menahem and Singh’s formula and Sorrells’ formula. *Geophysical Journal International*, 238(2): 820–826, 06 2024. doi: 10.1093/gji/ggae185.
- Tanimoto, T. and Valocin, A. Existence of the threshold pressure for seismic excitation by atmospheric disturbances. *Geophysical Research Letters*, 43(21):11,202–11,208, 2016. doi: 10.1002/2016GL070858.
- Tanimoto, T. and Wang, J. Theory for Deriving Shallow Elasticity Structure From Colocated Seismic and Pressure Data. *Journal of Geophysical Research: Solid Earth*, 124(6):5811–5835, June 2019. doi: 10.1029/2018JB017132.
- The ObsPy Development Team. ObsPy 1.2.1 [software], 2020. doi:

10.5281/zenodo.3706479.

- Tytell, J., Vernon, F., Hedlin, M., de Groot Hedlin, C., Reyes, J., Busby, B., Hafner, K., and Eakins, J. The USArray Transportable Array as a Platform for Weather Observation and Research. *Bulletin of the American Meteorological Society*, 97(4):603–619, Apr. 2016. doi: 10.1175/BAMS-D-14-00204.1.
- Uieda, L., Tian, D., Leong, W. J., Jones, M., Schlitzer, W., Toney, L., Grund, M., Yao, J., Magen, Y., Materna, K., Newton, T., Anant, A., Ziebarth, M., Quinn, J., and Wessel, P. PyGMT: A Python interface for the Generic Mapping Tools (v0.5.0) [software], 2021. doi: 10.5281/zenodo.5607255.
- U.S. Geological Survey Earthquakes Hazards Program. Advanced National Seismic System (ANSS) comprehensive catalog of earthquake events and products [dataset], 2017. doi: 10.5066/F7MS3QZH.
- Wald, D. J. and Allen, T. I. Topographic Slope as a Proxy for Seismic Site Conditions and Amplification. *Bulletin of the Seismological Society of America*, 97(5):1379–1395, Oct. 2007. doi: 10.1785/0120060267.
- Walker, K. T., Shelby, R., Hedlin, M. A. H., de Groot-Hedlin, C., and Vernon, F. Western U.S. Infrasonic Catalog: Illuminating infrasonic hot spots with the USArray. *Journal of Geophysical Research: Solid Earth*, 116(B12), 2011. doi: 10.1029/2011JB008579.
- Wang, J. and Tanimoto, T. Estimating Near-Surface Rigidity from Low-Frequency Noise Using Collocated Pressure and Horizontal Seismic Data. *Bulletin of the Seismological Society of America*, 110(4):1960–1970, Aug. 2020. doi: 10.1785/0120200098.
- Welch, P. The use of fast Fourier transform for the estimation of power spectra: A method based on time averaging over short, modified periodograms. *IEEE Transactions on Audio and Electroacoustics*, 15(2):70–73, 1967. doi: 10.1109/TAU.1967.1161901.
- Wills, G., Nippres, A., Green, D. N., and Spence, P. J. Site-Specific Variations in Air-to-Ground Coupled Seismic Arrivals from the 2012 October 16 Explosion at Camp Minden, Louisiana, United States. *Geophysical Journal International*, 231(1):243–255, June 2022. doi: 10.1093/gji/ggac184.
- Yong, A., Thompson, E., Wald, D., Knudsen, K., Odum, J., Stephenson, W., and Haefner, S. Compilation of VS30 Data for the United States: U.S. Geological Survey Data Series 978, 2016. doi: 10.3133/ds978.
- Zippenfenig, P. Open-Meteo.com Weather API [software], 2023. doi: 10.5281/zenodo.7970649.

The article *Alaska Upper Crustal Velocities Revealed by Air-to-Ground Coupled Waves From the 2022 Hunga Tonga–Hunga Ha’apai Eruption* © 2025 by Kenneth A. Macpherson is licensed under CC BY 4.0.